Appl. Phys. B 81, 1015–1047 (2005)
DOI: 10.1007/s00340-005-2036-6

Applied Physics B
Lasers and Optics

Invited paper

A. VOGEL[1,✉]
J. NOACK[1]
G. HÜTTMAN[1]
G. PALTAUF[2]

Mechanisms of femtosecond laser nanosurgery of cells and tissues

[1] Institut für Biomedizinische Optik, Universität zu Lübeck, Peter-Monnik Weg 4, 23562 Lübeck, Germany
[2] Institut für Physik, Karl-Franzens-Universität Graz, Universitätsplatz 5, 8010 Graz, Austria

Received: 9 September 2005
Published online: 15 November 2005 •

ABSTRACT We review recent advances in laser cell surgery, and investigate the working mechanisms of femtosecond laser nanoprocessing in biomaterials with oscillator pulses of 80-MHz repetition rate and with amplified pulses of 1-kHz repetition rate. Plasma formation in water, the evolution of the temperature distribution, thermoelastic stress generation, and stress-induced bubble formation are numerically simulated for NA = 1.3, and the outcome is compared to experimental results. Mechanisms and the spatial resolution of femtosecond laser surgery are then compared to the features of continuous-wave (cw) microbeams. We find that free electrons are produced in a fairly large irradiance range below the optical breakdown threshold, with a deterministic relationship between free-electron density and irradiance. This provides a large 'tuning range' for the creation of spatially extremely confined chemical, thermal, and mechanical effects via free-electron generation. Dissection at 80-MHz repetition rate is performed in the low-density plasma regime at pulse energies well below the optical breakdown threshold and only slightly higher than used for nonlinear imaging. It is mediated by free-electron-induced chemical decomposition (bond breaking) in conjunction with multiphoton-induced chemistry, and hardly related to heating or thermoelastic stresses. When the energy is raised, accumulative heating occurs and long-lasting bubbles are produced by tissue dissociation into volatile fragments, which is usually unwanted. By contrast, dissection at 1-kHz repetition rate is performed using more than 10-fold larger pulse energies and relies on thermoelastically induced formation of minute transient cavities with lifetimes < 100 ns. Both modes of femtosecond laser nanoprocessing can achieve a 2–3 fold better precision than cell surgery using cw irradiation, and enable manipulation at arbitrary locations.

PACS 42.62.Be; 72.20.Jv

Contents

✉ Fax: +49-451-500-6546, E-mail: vogel@bmo.uni-luebeck.de

1 Introduction

1.1 *Cell surgery*

Nonlinear absorption of short and ultra-short laser pulses focused through microscope objectives of high numerical aperture (NA) can be used to achieve very fine and highly localized laser effects inside biological media that are transparent at low irradiance [1–4] as well as in the bulk of photonic materials [5–8].

With moderate NAs and nanosecond (ns) laser pulses, this possibility was utilized in the 1980s for intraocular surgery [9, 10]. After the advent of femtosecond (fs) lasers, it was also employed for corneal intrastromal refractive surgery [11, 12] and for the creation of corneal flaps in excimer laser refractive surgery (LASIK) [11–14]. However, with moderate NAs, the spatial distribution of the deposited energy is influenced by nonlinear self-focusing, normal group-velocity dispersion, and plasma defocusing leading to filamentation and streak formation in the biological material [1, 7, 15–21]. Diffraction at the aperture of the optical system may also contribute to streak formation [22]. The nonlinear propagation effects become ever more important when the laser pulse duration is reduced and a larger laser power is required to produce optical breakdown. Therefore, it is not possible to achieve highly localized energy deposition when femtosecond pulses are focused into the bulk of transparent media at low NA. Plasma-mediated femtosecond laser nanoprocessing requires focusing at very large numerical apertures – not only to minimize the diffraction-limited focus diameter but also to avoid filamentation. Self-focusing occurs when a critical power is exceeded, regardless of which focusing angle is used. By contrast, optical breakdown requires an irradiance threshold to be surpassed. With increasing numerical aperture the spot size becomes smaller and thus the power that is necessary to overcome the threshold irradiance decreases. Beyond a certain numerical aperture, the breakdown power is smaller than the critical power for self-focusing, and localized energy deposition on a sub-micrometer scale can be achieved. For femtosecond optical breakdown in water and glass this was found to be the case for NA ≥ 0.9 [5].

Recent years have seen a continuous rise of interest in micro- and nanosurgery on a cellular and sub-cellular level. One important application is the separation of individual cells or other small amounts of biomaterial from heterogeneous tissue samples for subsequent genomic or proteomic analysis. Sensitive analytical techniques such as polymerase chain reaction (PCR) enable the analysis of very small amounts of materials [23–25], which allows for ever more specific investigations of cell constituents and their functions. Key technologies for sample preparation are laser microdissection (LMD) [26, 27] and subsequent laser pressure catapulting (LPC) of the dissected specimens into a vial for further analysis [28–31]. A related technique is laser-induced cell lysis and catapulting of the cell content into a micropipet for time-resolved capillary electrophoresis [32, 33]. Laser microbeams have also been applied to dissect chromosomes [34–37], fuse cells [38, 39], and for laser-assisted fertilization or hatching by ablation of the outer egg membrane (zona pellicula), a novel method for in-vitro fertilization [39–43]. Laser-induced transient permeabilization of the cell membrane is of great interest for a gentle transfection of genes and transfer of other substances into specific cell types [44–56].

Laser-generated inactivation of specific proteins or cell organelles together with an analysis of the induced deviations from the normal development provides information about the function of the respective proteins and organelles and can be utilized to study cell proliferation, embryonal development, or stress-induced reaction pathways. Two complementary strategies for functional studies have been followed. In the 'systemic' approach, specific proteins are targeted by means of antibodies attached to metallic nanoparticles or chromophores [57, 58]. When the antibody–absorber conjugates have bound to the target protein(s), the entire cell or group of cells is exposed to a short-pulsed laser beam. Protein inactivation occurs through linear absorption of the laser irradiation in the nanoparticles or chromophores, respectively, resulting in thermomechanical or photochemical destruction of the target proteins regardless of their localization within the cell [58–62]. In the 'local' approach, which is investigated in the present paper, one or a few specific target structures are irradiated by a tightly focused laser beam that dissects, alters, or inactivates the material within the focal region. When suitable laser parameters are used, the laser energy is deposited via nonlinear absorption, and surgery can be performed at any desired location within a cell or a small organism, regardless of its linear absorption properties.

1.2 *Historical development*

Historically, light inactivation of cells or cell organelles was first attempted in 1912 by Tschachotin using 280-nm irradiation from a magnesium spark imaged by a microscope objective on a 5-μm-wide spot on the cell [63]. This type of apparatus was highly refined in the 1950s by Bessis and Nomarski, and the resolution increased into the sub-micrometer regime [64, 65]. However, these instruments required very long exposure times. After the advent of the laser, a high-brightness light source was available that enabled the reduction of the exposure time into the microsecond range [66]. First experiments on mitochondrial inactivation were performed using free-running ruby-laser pulses with about 500-μs duration that were focused into a 5-μm spot [67, 68]. Later, chromosomal dissection was demonstrated using argon-laser irradiation with 20–30-μs duration [69, 70]. Owing to the good quality of the argon-laser beam and the shorter wavelength, it could be focused into a much smaller spot than the multimode emission of the initial ruby lasers. It is important to note that microsecond pulses are still 'long' in the context of cell surgery. We shall see in Sect. 5.3 that for large numerical apertures during pulses longer than about 10 μs a stationary temperature distribution similar to that produced by continuous-wave (cw) irradiation evolves around the laser focus. Long-pulsed irradiation from cw lasers is still used by various researchers [42, 47, 52, 56, 71], especially for cell-membrane permeabilization or perforation of the zona pellucida. A drawback of the quasi-cw irradiation is that the energy deposition is based on linear (i.e. one-photon) absorption and thus requires staining of target structures with vital dyes [67–69], unless laser powers larger than 1 W are used [70] or wavelengths are employed that are well absorbed even in unstained biological material [42, 56, 71].

Soon after the introduction of the laser microbeam, researchers also began to use short-pulsed laser irradiation, mostly with wavelengths in the UV region of the optical spectrum and with durations of a few nanoseconds [26–29, 34, 36, 38, 39, 48, 49, 51, 54, 72–75]. It was found that short laser pulses enable localized energy deposition at arbitrary locations without external sensitizing agents, even though the

ablation threshold can still be lowered by staining of the target structures [37, 49, 54, 76, 77]. With nanosecond pulses, energies between 0.25 μJ and 250 μJ were required to produce the desired ablative effect, depending on the laser wavelength, beam profile, numerical aperture, and the quality of the optical scheme used for coupling the laser beam into the microscope. Use of UV wavelengths that are well absorbed by biomolecules yielded lower ablation thresholds than the use of visible or near-IR irradiation under similar focusing conditions. Recently, it was demonstrated that pulsed laser microdissection relies on plasma formation supported by linear absorption, and that this is associated with violent mechanical effects (shock-wave emission and cavitation bubble formation) reaching well beyond the region of energy deposition [3, 31]. Pulse energies in the microjoule range typical for nanosecond laser microbeams can therefore severely affect the cell viability.

In the search for finer effects, researchers first employed picosecond (ps) pulses that could produce intracellular dissections with energies of 70–140 nJ [35, 78], and later femtosecond pulses that enabled them to lower the ablation threshold to an energy range between 0.4 nJ and a few nanojoules [4, 79]. Due to the low energy threshold for plasma formation [80, 81], femtosecond pulses can create very fine effects with a spatial extent below the optical diffraction limit. This has been demonstrated in chromosomes [4, 37], various other cell organelles [77, 82–85], small organisms [79, 86, 87], and tissues [55, 88, 89]. Sub-diffraction-limited resolution can be achieved because the nonlinear absorption diminishes the volume into which the laser energy is deposited. While for nanosecond pulses the optical breakdown threshold depends strongly on the linear absorption at the laser focus, femtosecond optical breakdown exhibits a much weaker dependence on the absorption coefficient of the target material [90]. This facilitates the targeting of arbitrary cellular structures. Because the wavelength dependence of femtosecond breakdown is weak [91], IR wavelengths that can penetrate deeply into the tissue can be used without compromising the precision of tissue effects as is the case with ns pulses [3, 48]. Moreover, when pulses from a fs oscillator are used, it becomes possible to combine nonlinear material modification with nonlinear imaging techniques based on two-photon fluorescence excitation or second-harmonic generation [53, 77, 79, 86, 88]. Additional progress was possible through the use of modern gene fusion products such as green fluorescent proteins (GFPs) which permit the visualization and ablation of cellular structures that are below the resolution of a light microscope [76, 79, 86, 92]. The above advances allow for an unprecedented precision of aiming, surgery, and the analysis of the created immediate and long-term effects. This potential of fs and ps pulses has been utilized in a variety of functional studies to elucidate the mechanisms of chromosome separation during cell division [35, 74, 78, 93], induce highly localized DNA damage [82], measure the biophysical properties of the cytoskeleton and mitochondria [85, 94], stimulate calcium waves in living cells [95], demonstrate nerve regeneration after axotomy within a living *C. elegans* worm [79], map thermosensation in *C. elegans* [87], and shed light on morphogenetic movements in embryonal development [34, 86].

1.3 *Objectives of the present study*

The high precision of the femtosecond laser effects is certainly related to the fact that the energy threshold for femtosecond optical breakdown is very low. Calculated breakdown energies for 100-fs pulses focused into water by an objective with NA = 1.3 are as small as 0.6 nJ at 355 nm, 1.6 nJ at 532 nm, and 3.9 nJ at 1064 nm [91]. The low breakdown threshold is, on the other hand, not sufficient to explain the fineness of the laser effects because laser-induced breakdown is generally associated with mechanical effects such as shock-wave emission and bubble formation that extend beyond the focal region [3, 80, 96]. We found in previous theoretical studies that plasmas with a large free-electron density are produced in a fairly large irradiance range below the breakdown threshold that was defined by a critical free-electron density $\varrho_{cr} = 10^{21}$ cm^{-3} [91, 97]. To understand the full potential of femtosecond pulses for highly localized material processing and modification of biological media, one therefore needs to include the irradiance range below the optical breakdown threshold. Moreover, one needs to elucidate why the conversion of absorbed laser light into mechanical energy above the breakdown threshold is much smaller than for longer pulse durations [2, 80].

The present study investigates the chemical, thermal, and thermomechanical effects arising from low-density plasmas to explain the mechanisms underlying femtosecond laser nanosurgery of cells and biological tissues. Two parameter regimes have been established for nanosurgery: one technique uses long series of pulses from fs oscillators with repetition rates of the order of 80 MHz and pulse energies well below the optical breakdown threshold that do not much exceed the energies used for nonlinear imaging [4, 37, 53, 55, 77, 86, 89, 95, 98]. The other approach uses amplified pulse series at 1-kHz repetition rate with pulse energies slightly above the threshold for transient bubble formation [79, 83–85]. To cover both regimes and to address possible side effects of nonlinear imaging, we investigate plasma formation and plasma-induced effects for an irradiance range reaching from the values used for nonlinear imaging to those leading to bubble formation. We consider repetition rates in the kilohertz range where the mechanical and thermal events induced by subsequent pulses are largely independent, and in the megahertz range where accumulative effects are likely to occur.

We use a rate-equation model considering multiphoton ionization, tunnel ionization, and avalanche ionization to numerically simulate the temporal evolution of the free-electron density during the laser pulse for a given irradiance, and to calculate the irradiance dependence of the free-electron density and volumetric energy density reached at the end of the laser pulse. The value of the energy density created by each laser pulse is then used to calculate the temperature distribution in the focal region after application of a single laser pulse and of series of pulses. The results of the temperature calculations yield, finally, the starting point for calculations of the thermoelastic stresses that are generated during the formation of the low-density plasmas, and of stress-induced bubble formation. All calculations are performed for a numerical aperture of NA = 1.3 and the wavelength of the titanium sapphire

laser ($\lambda = 800$ nm). Whenever possible, the findings of the numerical simulations are compared to experimental results.

The numerical calculations yield threshold values of the irradiance above which chemical changes in the focal region, a considerable temperature rise, and bubble formation are expected to occur. We found two different mechanisms of bubble formation: at repetition rates in the MHz range, fairly large long-lasting bubbles containing non-condensable gas can be formed by plasma-mediated accumulative heating and chemical disintegration of biomolecules. At lower repetition rates, transient bubbles with lifetimes below 100 ns are created by thermoelastic stresses. Due to the thermoelastic origin of bubble formation, the conversion efficiency from absorbed laser light energy into bubble energy is low, enabling the creation of spatially extremely confined disruptive effects.

A comparison between experimental parameters used for cell surgery and our numerical results revealed two different modes of femtosecond laser nanosurgery: dissection using long pulse trains at MHz repetition rates is mediated by free-electron-induced chemical decomposition (bond breaking) and not related to heating or thermoelastic stresses. With this dissection mode, bubble formation needs to be avoided because the relatively large and long-lasting bubbles cause dislocations far beyond the laser focus. By contrast, intracellular dissection at moderate (kHz) repetition rates relies on the thermoelastically induced formation of minute transient cavities. Both modes of femtosecond laser nanoprocessing of biomaterials achieve a better precision than cell surgery using cw irradiation.

Femtosecond-laser-produced low-density plasmas are thus a versatile tool for the manipulation of transparent biological media and other transparent materials such as glass. However, they may also be a potential source of damage in multiphoton microscopy and higher-harmonic imaging.

2 Plasma formation

2.1 *Qualitative picture*

The process of plasma formation through laser-induced breakdown in transparent biological media is schematically depicted in Fig. 1. It essentially consists of the formation of quasi-free electrons by an interplay of photoionization and avalanche ionization.

It has been shown experimentally that the optical breakdown threshold in water is very similar to that in ocular and other biological media [99]. For convenience, we shall therefore focus attention on plasma formation in pure water. Whereas the optical breakdown in gases leads to the generation of free electrons and ions, it must be noted that in condensed matter electrons are either bound to a particular molecule or they are 'quasi-free' if they have sufficient kinetic energy to be able to move without being captured by local potential energy barriers. Transitions between bound and quasi-free states are the equivalent of ionization of molecules in gases. To describe the breakdown process in water, Sacchi [100] has proposed that water should be treated as an amorphous semiconductor and the excitation energy Δ regarded as the energy required for a transition from the molecular $1b^1$ orbital into an excitation band (band gap 6.5 eV) [101–103]. We follow this approach. For simplicity, we will use the terms 'free electrons' and 'ionization' as abbreviations for 'quasi-free electrons' and 'excitation into the conduction band'. Nonlinear absorption of liquid water actually not only involves ionization but also dissociation of the water molecules [103], but in our model dissociation is neglected to reduce the complexity of the numerical code.

The photon energies at the wavelengths of 1064 nm, 800 nm, 532 nm, and 355 nm investigated in this study are 1.17 eV, 1.56 eV, 2.34 eV, and 3.51 eV, respectively. This means that the energy of six, five, three, and two photons, respectively, is required to overcome the band-gap energy $\Delta = 6.5$ eV. The excitation energy into the conduction band can be provided either by photoionization (multiphoton ionization or tunneling [104, 105]) or by impact ionization [106–109]. In previous breakdown models, it was often assumed that a free electron could be produced as soon as Δ was exceeded either by the sum of the simultaneously absorbed photons or by the kinetic energy of an impacting free electron [81, 110–112]. However, for very short laser pulses where breakdown occurs at large irradiance values, the band-gap energy has to be replaced by the effective ionization potential to account for the oscillation energy of the electron due to the electrical laser field. The ionization potential of individual atoms is [104]

$$\tilde{\Delta} = \Delta + \frac{e^2 F^2}{4m\omega^2}\,, \tag{1}$$

where ω and F denote the circular frequency and amplitude of the electrical laser field, e is the electron charge, and $1/m = 1/m_c + 1/m_v$ is the exciton reduced mass that is given by the effective masses m_c of the quasi-free electron in the conduction band and m_v of the hole in the valence band. The second term in (1) can be neglected in nanosecond optical

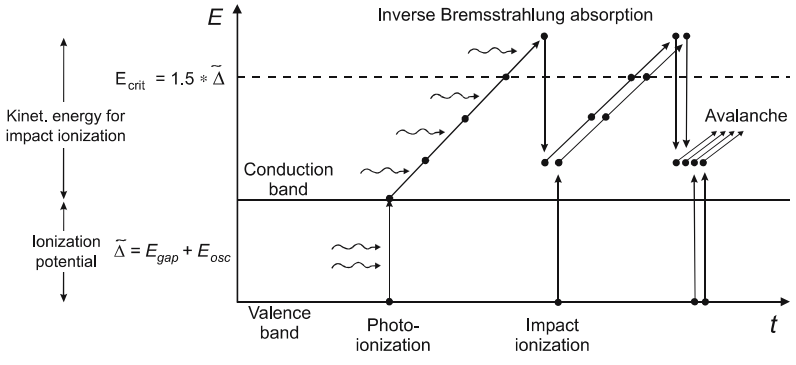

FIGURE 1 Interplay of photoionization, inverse Bremsstrahlung absorption, and impact ionization in the process of plasma formation. Recurring sequences of inverse Bremsstrahlung absorption events and impact ionization lead to an avalanche growth in the number of free electrons. The requirements to satisfy the conservation laws for energy and momentum in impact ionization, and their consequences for plasma formation, are discussed in the text

breakdown, but must be considered in femtosecond optical breakdown where F is orders of magnitude larger.

Multiphoton ionization (MPI) and tunneling are the mechanisms governing photoionization for different field strengths and frequencies of the electromagnetic field. In his classical paper [104], Keldysh introduced a parameter $\gamma = \omega/\omega_t$ to distinguish tunneling and MPI regimes. Here $1/\omega_t$ stands for the tunneling time through the atomic potential barrier, which is inversely proportional to the strength of the electromagnetic field. For values $\gamma \ll 1$ as obtained with low frequencies and large field strengths tunneling is responsible for ionization, while for values $\gamma \gg 1$ typical for optical frequencies and moderate field strengths the probability of MPI is much higher than that of tunneling. However, femtosecond optical breakdown requires very high field strengths for which the tunneling time through the atomic potential barrier is extremely short, leading to values $\gamma < 1$ of the Keldysh parameter even for optical frequencies. For $\lambda = 800$ nm, the transition from multiphoton to tunneling ionization occurs at field strengths of about 100–200 MV/cm, corresponding to irradiances of $1.3–2.6 \times 10^{13}$ W/cm^2 [21, 112, 113]. Values for the breakdown irradiance for a 100-fs pulse in distilled water (1.1×10^{13} W/cm^2 for $\lambda = 580$ nm [80]) are close to this transition. Approximations of the Keldysh theory considering only multiphoton ionization that were used in previous breakdown models [81, 110, 111] are thus inappropriate for the modeling of femtosecond breakdown, especially for pulse durations ≤ 100 fs.

Once a free electron is produced in the medium, it can absorb photons in a non-resonant process called 'inverse Bremsstrahlung' in the course of collisions with heavy charged particles (ions or atomic nuclei) [106]. A third particle (ion/atom) is necessary for energy and momentum to be conserved during absorption, as they cannot be both conserved if only an electron and a photon interact. The electron gains kinetic energy during the absorption of the photon. After a sequence of several inverse Bremsstrahlung absorption events, the kinetic energy is sufficiently large to produce another free electron through impact ionization [107–109, 113]. Two free electrons with low kinetic energies are now available, which can gain energy through inverse Bremsstrahlung absorption (Fig. 1). The recurring sequence of inverse Bremsstrahlung absorption events and impact ionization leads to an avalanche growth in the number of free electrons if the irradiance is high enough to overcome the losses of free electrons through diffusion out of the focal volume and through recombination. The energy gain through inverse Bremsstrahlung must, moreover, be more rapid than the energy loss by collisions with heavy particles occurring without simultaneous absorption of a photon (the fraction of energy lost is proportional to the ratio of the electron and ion masses). The whole process is called 'avalanche ionization' or 'cascade ionization'.

For impact ionization to occur, the kinetic energy of the impacting electron must be larger than the effective ionization potential $\tilde{\Delta}$ to satisfy the conservation laws for energy and momentum [109, 114]. According to Ridley [109], the critical energy for bands with parabolic energy dispersion is

$$E_{\text{crit}} = \left(\frac{1+2\mu}{1+\mu}\right)\tilde{\Delta}\,, \text{ with } \mu = \frac{m_c}{m_v}\,. \tag{2}$$

The value of μ depends on the band structure; it is 1 for a symmetric band structure with the Fermi level at the center of the band gap but smaller for semiconductors [109]. Kaiser et al. assumed that $\mu = 1$ for α-SiO_2 [113], and since we did not find information on the value of μ for water, we follow their assumption. This implies that a kinetic energy of $E_{\text{crit}} = 1.5\tilde{\Delta}$ is required for impact ionization [113, 115].

The excess energy of $0.5\tilde{\Delta}$ that remains after impact ionization is distributed among the collision partners [109, 113, 116]. Thus, each quasi-free electron produced by impact ionization has to gain less energy than $1.5\tilde{\Delta}$ to reach the critical energy. However, the average energy leading to an impact ionization event is larger than E_{crit} because the impact ionization rate increases with kinetic energy [108, 113–115]. To consider both factors, we assume that the average energy gain required for a free electron to cause impact ionization is $1.5\tilde{\Delta}$, as illustrated in Fig. 1. A more detailed consideration of the energy distribution of the free-electron population and of the energy dependence of the ionization rates [108, 113, 115, 116] would require experimental data on collision cross sections that are not available for water.

While strong-field ionization is almost 'instantaneous', there are time constraints on cascade ionization because several consecutive inverse Bremsstrahlung absorption events are necessary for a free electron to pick up the critical energy for impact ionization. For a band gap of 6.5 eV in water and a Keldysh parameter $\gamma = 2$, the effective ionization potential is $\tilde{\Delta} \approx 7.3$ eV, and the average gain in kinetic energy required to enable impact ionization is $(3/2)\tilde{\Delta} \approx 10.95$ eV. When laser irradiation of $\lambda = 800$-nm wavelength with a photon energy of 1.55 eV is used to produce optical breakdown, an electron must undergo at least eight inverse Bremsstrahlung absorption events before impact ionization can occur. As mentioned above, inverse Bremsstrahlung absorption can only occur during collisions of the electrons with heavy particles. In condensed matter, the time τ between collisions was estimated to be roughly 1 fs [117]. Recent experimental investigations yielded a value of $\tau = 1.7$ fs for fused silica [118]. Based on this value, the minimum time for one doubling sequence of the number of free electrons by cascade ionization is 13.6 fs even if every collision involves absorption of a photon. A detailed analysis of the time constraints in cascade ionization was presented by Kaiser et al. [113] and Rethfeld [115]. They came to the conclusion that cascade ionization plays only a minor role in femtosecond breakdown compared to multiphoton effects – in striking contrast to Joglekar et al. [119, 120], who presented some experimental evidence for the opposite statement. However, the time constraints in cascade ionization were not considered in the models presented by Joglekar et al. and other authors who claim that cascade ionozation dominates femtosecond breakdown [112, 119, 120].

In our study, we shall combine the Keldysh model for strong-field ionization (including both tunneling and multiphoton absorption) [104] with Shen's, Kennedy's, and Stuart's description of avalanche ionization [1, 110, 116], which is based on the Drude model. Other recent studies of femtosecond optical breakdown in transparent dielectrics have followed the same approach [21, 121], while Tien et al. [112]

combined the Keldysh theory with Thornber's model of avalanche ionization [107]. Since the numerical model used by Kaiser et al. [113] and Rethfeld [115] is very complex, we consider the time constraints in cascade ionization by simply introducing a retarded time for the calculation of the cascade ionization rates, as described in Sect. 2.2.

To obtain a better understanding of the mechanisms of cell surgery using femtosecond pulses, we are interested in the plasmas below and slightly above the optical breakdown threshold. It is evident that a precise delineation of the corresponding irradiance range requires a clear definition of the breakdown threshold. When nano- and picosecond pulses are employed, optical breakdown is accompanied by the formation of a luminous plasma and followed by shock-wave emission and cavitation [15, 96]. At these pulse durations, the plasma luminescence usually serves as an experimental breakdown criterion [3, 15]. With shorter laser pulses, there is no plasma luminescence in the visible region of the spectrum, and breakdown in aqueous media is usually detected by observing the formation of a cavitation bubble [81, 122]. By contrast, in theoretical investigations the breakdown threshold is defined by the irradiance (or energy) required to produce a certain critical free-electron density ϱ_{cr} at the laser focus. Mostly, the electron density

$$\varrho'_{\mathrm{cr}} = \omega^2 \frac{m_{\mathrm{c}} \varepsilon_0}{e^2}\,, \tag{3}$$

above which the plasma becomes both strongly reflective and absorbing, is used as breakdown criterion [18, 112, 113, 116, 123]. Here ε_0 denotes the vacuum dielectric permittivity. The critical electron density ϱ'_{cr} amounts to $0.984 \times 10^{21}\,\mathrm{cm}^{-3}$ for $\lambda = 1064\,\mathrm{nm}$, to $3.94 \times 10^{21}\,\mathrm{cm}^{-3}$ for $\lambda = 532\,\mathrm{nm}$, and to $8.86 \times 10^{21}\,\mathrm{cm}^{-3}$ for 355 nm, respectively. We use a free-electron density of $\varrho_{\mathrm{cr}} = 10^{21}\,\mathrm{cm}^{-3}$ as breakdown criterion in our numerical simulations of plasma formation. A constant value was chosen because the experimental threshold criterion (bubble formation) relates to a fixed value of the plasma energy density. In Sect. 6.3, threshold values obtained on this basis will be compared with experimental data and calculated values for the onset of stress-induced bubble formation.

Since all calculations are performed for a numerical aperture of NA = 1.3, nonlinear propagation effects in the biological medium can be neglected in the simulations of plasma formation, even for pulse durations as short as 100 fs, because Schaffer et al. showed that these nonlinear effects influence the breakdown threshold only for NA < 0.9 [5]. For NA > 0.9, self-focusing and filamentation may play a role well above the breakdown threshold, but are not relevant for the pulse energies used in nanosurgery on cells.

In this study, we restrict the modeling to optical breakdown in pure water. In real biological media, the band structure of water is modified by the presence of biomolecules in physiological solution with additional energy levels that may enhance both linear and nonlinear absorption processes. These modifications may lead to a lower threshold for plasma-mediated laser ablation and dissection, especially when exogeneous linearly absorbing dyes are used [37, 49, 54, 76, 77]. The consideration of these modifications will be the topic of future work.

2.2 *Numerical simulations*

The time evolution of the electron density ϱ_{c} in the conduction band under the influence of the laser light was calculated using a rate equation of the generic form [81]

$$\frac{\mathrm{d}\varrho}{\mathrm{d}t} = \eta_{\mathrm{photo}} + \eta_{\mathrm{casc}}\varrho_{\mathrm{c}} - \eta_{\mathrm{diff}}\varrho_{\mathrm{c}} - \eta_{\mathrm{rec}}\varrho_{\mathrm{c}}^2\,. \tag{4}$$

The first term represents the production of free electrons mediated by the strong electric field in the laser focus (photoionization via multiphoton and tunneling ionization), the second term represents the contribution of cascade ionization, and the last two terms describe the losses through diffusion of electrons out of the focal volume and recombination. The cascade ionization rate η_{casc} and the diffusion loss rate η_{diff} are proportional to the number of already produced free electrons, while the recombination rate η_{rec} is proportional to ϱ_{c}^2, as it involves an interaction between two charged particles (an electron–hole pair). Even though diffusion and recombination do not play a significant role during femtosecond laser pulses, they were included to enable a comparison with plasma formation by nanosecond pulses.

The temporal evolution of the electron density, $\varrho(t)$, was calculated for laser pulses with a Gaussian time variation [81], focused into pure water at a numerical aperture of NA = 1.3. At room temperature the initial steady-state free-electron density in the conduction band resulting from the Boltzmann distribution is negligible. Thus, the steady-state electron density in the ground state corresponds to the total electron density $\varrho_{\mathrm{v}} = 6.68 \times 10^{23}\,\mathrm{cm}^{-3}$ [110]. For photon energies below the ionization potential, free electrons have to be generated by multiphoton or tunnel ionization. The time-averaged ionization rate for a field with angular frequency ω and intensity I acting on an electron density $\varrho_{\mathrm{v}} - \varrho_{\mathrm{c}}$ in the ground state was derived by Keldysh [104] to be

$$\begin{aligned}\left(\frac{\mathrm{d}\varrho_{\mathrm{c}}}{\mathrm{d}t}\right)_{\mathrm{photo}} &= \frac{2\omega}{9\pi}\left(\frac{\sqrt{1+\gamma^2}}{\gamma}\frac{m\omega}{\hbar}\right)^{3/2} \\ &\times Q\left(\gamma, \frac{\tilde{\Delta}}{\hbar\omega}\right) \times (\varrho_{\mathrm{v}} - \varrho_{\mathrm{c}}) \exp\left\{-\pi\left\langle\frac{\tilde{\Delta}}{\hbar\omega}+1\right\rangle\right. \\ &\left.\times\left[K\left(\frac{\gamma}{\sqrt{1+\gamma^2}}\right) - E\left(\frac{\gamma}{\sqrt{1+\gamma^2}}\right)\right] \Big/ E\left(\frac{1}{\sqrt{1+\gamma^2}}\right)\right\}\,,\end{aligned}$$

where

$$\begin{aligned}Q(\gamma, x) &= \sqrt{\pi \Big/ 2K\left(\frac{1}{\sqrt{1+\gamma^2}}\right)} \\ &\times \sum_{l=0}^{\infty} \exp\left\{-\pi l\left[K\left(\frac{\gamma}{\sqrt{1+\gamma^2}}\right) - E\left(\frac{\gamma}{\sqrt{1+\gamma^2}}\right)\right]\right. \\ &\left.\Big/ E\left(\frac{1}{\sqrt{1+\gamma^2}}\right)\right\} \times \Phi\left\{\left[\pi\left(2\langle x+1\rangle - 2x + l\right)\right.\right. \\ &\left.\left.\Big/ 2K\left(\frac{1}{\sqrt{1+\gamma^2}}\right) E\left(\frac{1}{\sqrt{1+\gamma^2}}\right)\right]^{1/2}\right\}\,.\end{aligned} \tag{5}$$

Here $\langle x \rangle$ represents the integer part of the number x, $K()$ and $E()$ denote elliptic integrals of the first and second kinds, and $\Phi()$ denotes the Dawson probability integral

$$\Phi(z) = \int_0^z \exp\left(y^2 - x^2\right) \mathrm{d}y \,. \tag{6}$$

The Keldysh parameter γ and the effective ionization potential $\tilde{\Delta}$ for creating an electron–hole pair in condensed matter exhibiting a band structure are given by

$$\gamma = \frac{\omega}{e}\sqrt{\frac{c\varepsilon_0 m \Delta}{4I}} \text{ and } \tilde{\Delta} = \frac{2}{\pi}\Delta\frac{\sqrt{1+\gamma^2}}{\gamma}E\left(\frac{1}{\sqrt{1+\gamma^2}}\right) . \tag{7}$$

Some authors [110, 113, 115, 120] used the expression in (1) for the ionization potential of individual atoms to describe photoionization in condensed matter instead of the more adequate equation (7), which Keldysh derived for solids. For $\gamma \gg 1$, (5) reduces to the expression for multiphoton ionization used in [81, 110], and the ionization potential can be approximated by the band-gap energy Δ. Under these circumstances the photoionization rate shows an intensity dependence proportional to I^k, k representing the number of photons required to cross the band gap.

Figure 2 shows the calculated ionization rate for 780 nm as a function of the Keldysh parameter calculated with the complete model in (5) and with various approximations. For values $\gamma \ll 1$, the Keldysh multiphoton approximation predicts photoionization rates that are too low by several orders of magnitude, while the predictions of Kennedy's multiphoton approximation [81, 110] are by several orders of magnitude too large.

As soon as free electrons exist in the interaction volume, they gain kinetic energy through inverse Bremsstrahlung absorption of photons and can generate further free electrons through impact ionization once their energy exceeds the critical energy described by (2). As explained above, we assume that the average gain of kinetic energy by each electron required to cause an impact ionization event is $E = (3/2)\tilde{\Delta}$. The ionization rate per electron participating in the cascade is then

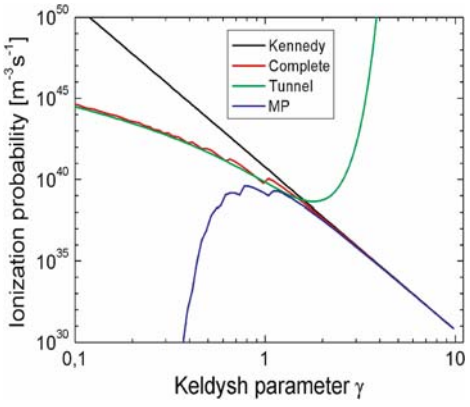

FIGURE 2 Nonlinear photoionization rate for water at $\lambda = 780$ nm calculated with the complete Keldysh model (*pink*), with Keldysh's approximations in the tunnel limit (*green*) and the multiphoton limit (*violet*), and with Kennedy's approximation in the multiphoton limit (*blue*) [81, 110]

given by [110]

$$\eta = \frac{1}{\omega^2\tau^2 + 1}\left[\frac{e^2\tau}{cn_0\varepsilon_0 m_\mathrm{c}(3/2)\tilde{\Delta}}I - \frac{m_\mathrm{c}\omega^2\tau}{M}\right] , \tag{8}$$

where τ is the time between collisions, c the vacuum speed of light, and n_0 the refractive index of the medium at frequency ω. The masses of the electron and the water molecule are m and M, respectively. For large irradiances, the cascade ionization rate is proportional to I.

Two aspects must still be considered to accurately determine the cascade contribution to the free-electron density. First, at least one free 'seed' electron produced by photoionization is required for the start of the cascade. Therefore, cascade ionization is only considered if there is at least a 50% probability of having this start electron in the focal volume. Second, it must be taken into account that inverse Bremsstrahlung absorption requires a finite time $\tau_\mathrm{ion} = \tau n$, which is determined by the mean free time τ (1.7 fs [118]) between electron/molecule collisions and the number n of photons that must be absorbed to gain sufficient energy. Therefore, the contribution of cascade ionization at time t must be evaluated using the electron density created at time $t_\mathrm{ret} = t - t_\mathrm{ion}$. A first-order approximation of this retardation of the cascade leads to the expression

$$\left(\frac{\mathrm{d}\varrho_\mathrm{c}}{\mathrm{d}t}\right)_\mathrm{casc} = \begin{cases} \frac{\eta}{1+\eta_\mathrm{ret}}\varrho_\mathrm{c} & \text{for } \varrho_\mathrm{c}V \geq 0.5 \,, \\ 0 & \text{for } \varrho_\mathrm{c}V < 0.5 \,. \end{cases} \tag{9}$$

Free electrons are lost in the interaction volume by diffusion out of the volume V and through recombination. The focal volume was assumed to be ellipsoidal, which corresponds to illumination of the rear aperture of the microscope objective with a plane wave, as will be discussed in Sect. 3.1. Thus, $V = (4/3)\pi a^2 b$, where a and b are the short and long half-axes of the ellipsoidal free-electron distribution described by (16), below. The resulting (negative) ionization rate due to diffusion is [110, 124]

$$\left(\frac{\mathrm{d}\varrho_\mathrm{c}}{\mathrm{d}t}\right)_\mathrm{diff} = -\frac{\tau E_\mathrm{av}}{3m\Lambda^2} \times \varrho_\mathrm{c} = -\frac{\tau 5\tilde{\Delta}}{6m_\mathrm{c}}\left[\frac{6}{a^2} + \frac{2}{b^2}\right] \times \varrho_\mathrm{c} \,, \tag{10}$$

where E_av is the average kinetic energy of the free electrons and Λ is the characteristic diffusion length. Free electrons produced by impact ionization possess, on average, a start energy of $(1/2)\tilde{\Delta}$ and produce another free electron through collisional ionization when they reach a kinetic energy of $2\tilde{\Delta}$. Thus, their mean kinetic energy is $(5/4)\tilde{\Delta}$, leading to the expression on the right-hand side of (10). For the recombination rate, we used an empirical value that was determined by Docchio through inspection of the decay of the plasma luminescence [125]:

$$\left(\frac{\mathrm{d}\varrho_\mathrm{c}}{\mathrm{d}t}\right)_\mathrm{rec} = -2 \times 10^{-9}\,\mathrm{cm}^3/\mathrm{s} \times \varrho_\mathrm{c}^2 \,. \tag{11}$$

In reality, recombination of free electrons in water is not a one-step process but consists in hydration of the electron within about 300 fs and subsequent decay of the hydrated state that has an average lifetime of ≈ 300 ns [103].

To obtain the evolution of the free-electron density during a Gaussian laser pulse

$$I(t) = I_0 \exp\left[-4\ln 2\left(\frac{t}{\tau_L}\right)^2\right], \tag{12}$$

the total rate equation

$$\frac{d\varrho_c}{dt} = \left(\frac{d\varrho_c}{dt}\right)_{photo} + \left(\frac{d\varrho_c}{dt}\right)_{casc} + \left(\frac{d\varrho_c}{dt}\right)_{diff} + \left(\frac{d\varrho_c}{dt}\right)_{rec} \tag{13}$$

was solved numerically for various laser pulse peak intensities I using a Runge–Kutta method with adaptive step-size control. Separate book-keeping was used for the contribution of (5) to evaluate the influence of multiphoton and cascade ionization. The breakdown threshold is defined as the irradiance I_{rate} required to produce a maximum electron density ϱ_{max} during the laser pulse that equals the critical density $\varrho_{cr} = 10^{21}\,cm^{-3}$. Besides the time evolution of the electron density, we also assessed the dependence of the maximum electron density on irradiance, by calculating ϱ_{max} as a function of I/I_{rate}.

2.3 *Evolution of free-electron density and breakdown thresholds*

The top row of Fig. 3 presents the evolution of the free-electron density ϱ_c during the laser pulse at the optical breakdown threshold for 6-ns, 1064-nm pulses, and for 100-fs, 800-nm pulses. To facilitate a comparison between the different pulse durations, the time t is normalized with the respective laser pulse duration τ_L. The contribution of photoionization to the total free-electron density is plotted as a dotted line. The bottom row of Fig. 3 shows how the maximum free-electron density achieved during the laser pulse depends on irradiance.

It is obvious that the dynamics of plasma formation is extremely different for nanosecond and femtosecond pulses. With nanosecond pulses, no free electrons are formed for irradiance values below the optical breakdown threshold because the irradiance is too low to provide seed electrons by means of multiphoton ionization (Fig. 3c). Once the irradiance is high enough to provide a seed electron, the ionization cascade can start. It proceeds very rapidly owing to the high irradiance (Fig. 3a). The electron density shoots up by nine orders of magnitude within a small fraction of the laser pulse duration until its rise is stopped by recombination, which is proportional to ϱ_c^2. The breakdown threshold is, hence, extremely sharp – either a highly ionized plasma is produced, or no plasma at all. These numerical predictions are supported by the experimental observation that at the threshold of nanosecond optical breakdown with IR laser pulses the transmission of the focal volume drops abruptly to less than 50% of the value without plasma formation [126, 127]. The transmission loss for shorter pulse durations is much less abrupt [80, 126–128].

With femtosecond pulses, a much higher irradiance is necessary for optical breakdown to be completed during the laser pulse duration than with nanosecond pulses. This favors the generation of free electrons through multiphoton ionization because of its stronger irradiance dependence – $\propto I^k$ as opposed to $\propto I$ for the cascade ionization rate (see Sect. 2.2). While with nanosecond pulses the total number of free electrons generated through avalanche ionization is 10^9 times larger than the number generated through multiphoton ionization (Fig. 3a), it is only 12 times larger with 100-fs pulses at 800 nm (Fig. 3b). As a consequence of the increasing importance of multiphoton ionization with shorter pulse durations, there is never a lack of seed electrons for avalanche ionization. An avalanche is initiated at irradiance values considerably lower than the breakdown threshold. The free-electron density reached at the end of the avalanche depends on irradiance

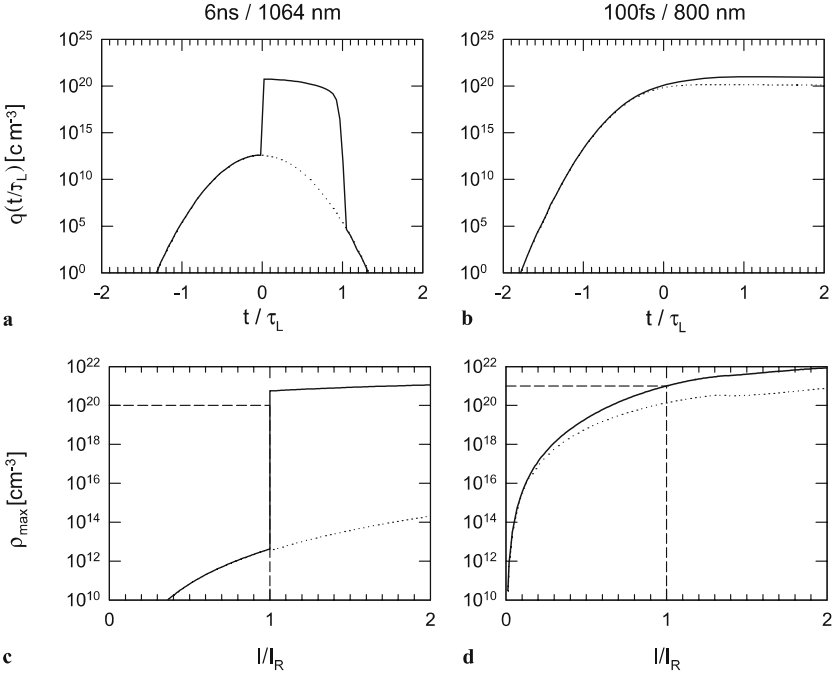

FIGURE 3 *Top row*: evolution of the free-electron density during the laser pulse at the optical breakdown threshold for 6-ns, 1064-nm pulses and for 100-fs, 800-nm pulses. The time t is normalized with respect to the laser pulse duration τ_L. The contribution of multiphoton ionization to the total free-electron density is plotted as a *dotted line*. *Bottom row*: maximum free-electron density ϱ_{max} achieved during the laser pulse as a function of irradiance, for the same laser parameters. The irradiance I is normalized with respect to the threshold irradiance I_{rate}. The threshold I_{rate} and the corresponding value of ϱ_{max} are marked by *dashed lines*

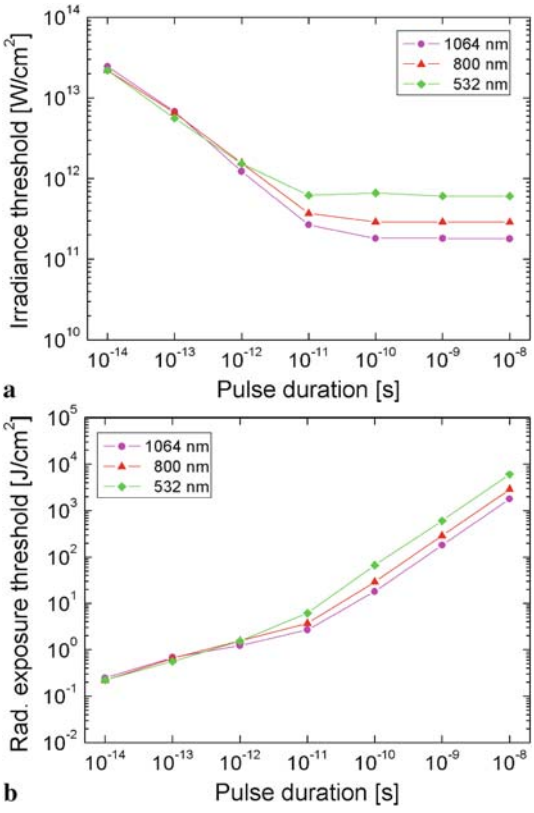

FIGURE 4 Calculated optical breakdown thresholds ($\varrho_{cr} = 10^{21}$ cm^{-3}) as a function of laser pulse duration for various laser wavelengths. (**a**) Irradiance thresholds, (**b**) radiant exposure thesholds

in a much smoother way (Fig. 3d) than for ns pulses (Fig. 3c). Therefore, one can generate any desired free-electron density by selecting an appropriate irradiance value.

Figure 4 presents threshold values for irradiance, I_{rate}, and radiant exposure, $F_{rate} = I_{rate} \times \tau_L$, required to reach a critical free-electron density of $\varrho_{cr} = 10^{21}$ cm^{-3}. The thresholds were calculated for various wavelengths and pulse durations ranging from 10 fs to 10 ns. Two regimes can be distinguished: for $\tau_L < 10$ ps, the threshold radiant exposure F_{rate} exhibits only a weak dependence on pulse duration. This reflects the fact that recombination plays only a minor role during ultra-short laser pulses. Therefore, only one set of free electrons is produced that corresponds to an approximately constant energy density within the focal volume. This is in accordance with the experimental threshold criterion of bubble formation that requires a specific energy density, which varies little with laser parameters. By contrast, for longer pulses more than one set of free electrons is produced and they recombine during the laser pulse. Here it is the threshold irradiance I_{rate} that remains approximately constant, because a minimum irradiance is required to provide the seed electrons for the ionization cascade by multiphoton ionization and to drive the cascade sufficiently fast to reach the critical free-electron density within the laser pulse duration. As a consequence of the constant threshold irradiance, the radiant exposure threshold and plasma energy density increase steeply with increasing pulse duration.

The predicted form of the $F_{rate}(\tau_L)$ dependence qualitatively matches experimental observations of the pulse-duration dependence of single-shot damage thresholds at surfaces of transparent large-band-gap dielectrics [112, 129] and ablation thresholds of corneal tissue [13, 130]. However, studies in which single-shot thresholds at longer pulse durations are mixed with multiple-shot thresholds at ultra-short durations show a steeper $F_{rate}(\tau_L)$ dependence for $\tau_L < 10$ ps both in corneal tissue [131, 132] and dielectrics [116, 123]. The lower thresholds with multiple exposures are due to accumulative effects, the possibility of which is explained by the smooth $\varrho_{max}(I/I_{rate})$ dependence shown in Fig. 3d.

The predicted wavelength dependence in the picosecond and nanosecond regimes (increasing threshold with decreasing wavelength) seems to be a little surprising at first sight, because multiphoton processes occur more easily at shorter wavelengths. However, one needs to keep in mind that the cascade ionization rate increases approximately proportionally to the square of the laser wavelength, as evident from (8).

2.4 *Low-density plasmas in bulk media*

Our numerical calculations for femtosecond breakdown in bulk transparent media indicate that it is possible to create low-density plasmas in which the energy density remains below the level that leads to cavity formation in the medium. Experimental evidence for the existence of low-density plasmas was recently provided by Mao et al. [18] through measurements of the free-electron density in MgO and SiO_2. Free electrons are produced in a fairly large irradiance range below the optical breakdown threshold, with a deterministic relationship between free-electron density and irradiance. Low-density plasmas thus offer the possibility to deliberately produce chemical changes, heating, and thermomechanical effects by varying the irradiance. These effects are very well localized because of the nonlinearity of the plasma-formation process, which, for sufficiently small irradiances, allows us to produce a plasma in a volume that is smaller than the diffraction-limited focus.

For larger irradiances, plasmas in bulk media grow beyond the region of the beam waist, which is not possible for plasma formation at surfaces [116, 120, 121]. At surfaces, the energy deposition becomes confined to a thin layer of less than 100-nm thickness once the free-electron density reaches the critical density, because the superficial plasma layer is highly absorbing and reflecting [116, 121, 133–135]. By contrast, in bulk media there is no restriction for the region of optical breakdown to spread towards the incoming laser beam with increasing irradiance. At large irradiances, breakdown starts to occur before the femtosecond pulse reaches the beam waist, and both irradiance and beam propagation are influenced by the plasma generation [21, 136]. These effects shield the focal region, enlarge the size of the breakdown region, and limit the free-electron density and energy density reached in the entire breakdown volume [21, 80, 137–139]. Low-density plasmas can, therefore, easily be produced in bulk media while at surfaces the self-induced confinement of plasma formation to a thin layer leads to a rapid rise of free-electron density with irradiance, and the irradiance range in which low-density plasmas can be formed is very small [116, 120].

The desired chemical or physical effects of low-density plasmas can be precisely selected if the slope of the $\varrho_{max}(I/I_{rate})$ curve is small because that offers a large

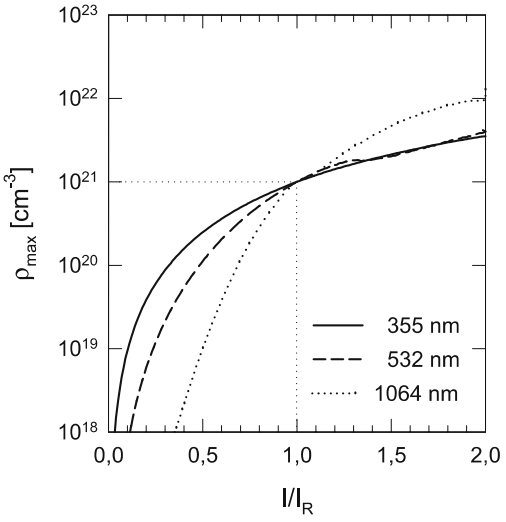

FIGURE 5 Maximum free-electron density as a function of irradiance, $\varrho_{\max}(I/I_{\text{rate}})$, for 100-fs pulses at 1064-nm, 532-nm, and 355-nm wavelengths. The normalized threshold ($I/I_{\text{rate}} = 1$) and the corresponding value of $\varrho_{\max}$ are marked by *dotted lines*

'tuning range' of the irradiance for each effect. Figure 5 shows that the tuning range increases for shorter laser wavelengths.

3 Irradiance and free-electron distributions within the focal volume

3.1 *Shape of the focal volume*

The temperature and stress distribution in the focal region depend on the distribution of quasi-free electrons produced during femtosecond optical breakdown. Therefore, we must first explore the shape of the irradiance and free-electron density distributions within the focal volume before we can investigate the resulting temperature and stress effects. Because of the nonlinearity of the breakdown process, the free-electron distribution is narrower than the irradiance distribution in the focal volume. A description of their relation will thus also allow us to estimate the possible increase of the spatial precision of the laser effects beyond the level achievable with techniques that are based on linear absorption.

The irradiance distribution in the focal volume of a diffraction-limited optical system for a focusing angle of $\alpha = 45°$ is reproduced in Fig. 6 from the textbook of Born and Wolf [140] (α is the half-angle of the light cone such as used in the definition of the numerical aperture $\text{NA} = n_0 \sin\alpha$). The isophotes (contour lines for equal irradiance) reveal that the focal volume in the center of the focal region has an approximately ellipsoidal shape. A similar structure was obtained experimentally when the irradiance distribution in a confocal laser scanning microscope (CLSM) was measured by scanning the tip of a scanning near field optical microscope (SNOM) through the focal region (Fig. 7), and by a surface-plasmon-based beam-profiling technique [141]. For our numerical simulations, the focal volume will therefore be approximated by an ellipsoid with short axis d and long axis l.

The short axis d of the ellipsoid is identified with the diameter of the central maximum of the Airy pattern in the focal plane that is given by

$$d = 1.22\frac{\lambda}{\text{NA}}\,. \tag{14}$$

The symbol λ refers to the vacuum wavelength of light. The refractive index of the medium is contained in the value of the numerical aperture (NA) of the microscope objective. The ratio l/d of the long and short axes can be obtained from the

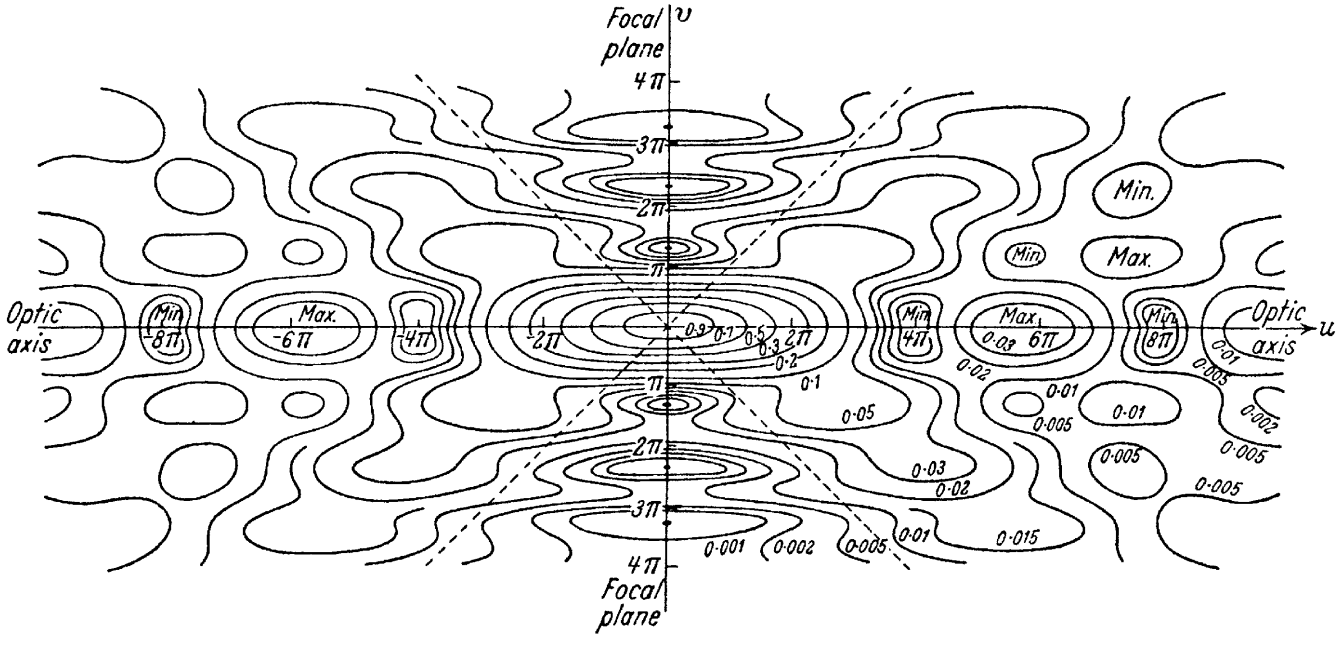

FIGURE 6 Isophotes (contour lines for equal irradiance) in the focal region of a diffraction-limited microscope objective used to focus a plane wave. The *dashed lines* represent the boundary of the geometrical focus. The focusing angle of $\alpha = 45°$ corresponds to a numerical aperture of NA = 0.94 in water. When the figure is rotated around the u axis, the minima on the v axis generate the Airy dark rings. The figure is taken from Ref. [140], p. 440

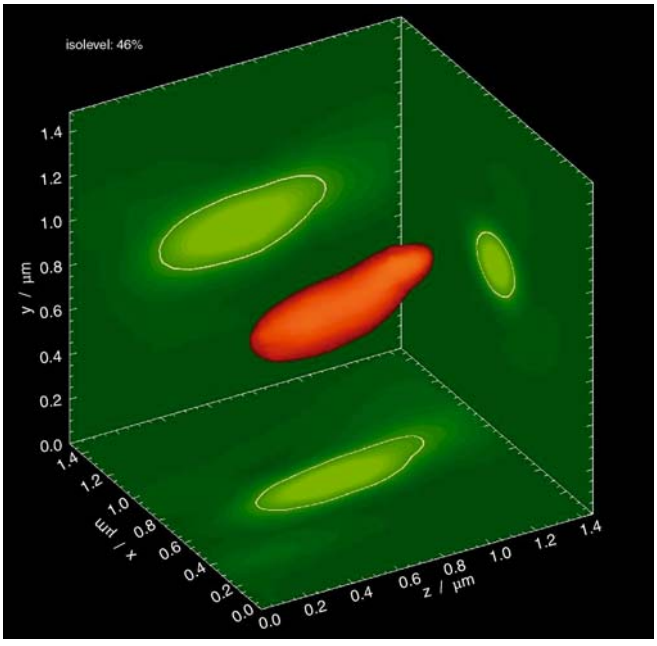

FIGURE 7 Irradiance distribution in a confocal laser scanning microscope measured by scanning the tip of a scanning near field optical microscope through the focal region of a Zeiss axiovert 100/C-Apo ×40 NA = 1.2 water-immersion microscope objective. The measurement was performed for a laser wavelength of $\lambda = 488$ nm; the isocontour lines refer to 46% of the maximum irradiance (courtesy of Volker Jüngel and Tilo Jankowski, Carl Zeiss Jena)

relation

$$\frac{l}{d} = \frac{1-\cos\alpha}{(3-2\cos\alpha-\cos 2\alpha)^{1/2}}\,, \tag{15}$$

which was derived by Grill and Stelzer for optical setups with very large solid angles [142]. For NA = 1.3, which in water corresponds to an angle of $\alpha = 77.8°$, we find $l/d = 2.4$. A similar value is also obtained from the experimental data in Fig. 7. For $\lambda = 800$ nm, the above considerations yield focal dimensions of $d = 750$ nm and $l = 1800$ nm.

3.2 *Irradiance and electron-density distributions within the focal volume*

The mathematical form of the diffraction-limited irradiance distribution in the Fraunhofer diffraction pattern of a microscope objective (Fig. 6) is too complex for convenient computation of the temperature and stress evolution induced by optical breakdown. We approximate the ellipsoidal region of high irradiance in the focus by a Gaussian function

$$I(r,z) = I(0,0)\exp\left[-2\left(\frac{r^2}{a^2}+\frac{z^2}{b^2}\right)\right], \tag{16}$$

where r and z are the coordinates in radial and axial directions, respectively, and $a = d/2$ and $b = l/2$ denote the short and long axes of the ellipsoid. The boundaries of the ellipsoid correspond to the $1/e^2$ values of the Gaussian irradiance distribution.

To derive the free-electron distribution $\varrho_{\max}(r,z)$ from the irradiance distribution $I(r,z)$, we assume that for femtosecond pulses the free-electron density at the end of the laser pulse is approximately proportional to I^k, where k is the number of photons required for multiphoton ionization. This simplifying assumption corresponds to the low-intensity approximation of the Keldysh theory and neglects the weaker irradiance dependence of avalanche ionization that usually dominates plasma formation during the second half of a laser pulse (Fig. 3b). For $\varrho_{\max} \le 5\times10^{20}\,\mathrm{cm}^{-3}$, the proportionality $\varrho_{\max} \propto I^k$ has been confirmed by the experimental results of Mao et al. [18]. The spatial distribution of the free-electron density can thus be expressed as

$$\varrho_{\max}(r,z) = \varrho_{\max}\left[I(0,0)\right]\exp\left[-2k\left(\frac{r^2}{a^2}+\frac{z^2}{b^2}\right)\right]. \tag{17}$$

Figure 8 shows the irradiance and electron-density distributions in the focal region according to (16) and (17) for NA = 1.3 and $\lambda = 800$ nm, for which $k = 5$. Due to the nonlinear absorption process underlying optical breakdown, the free-electron distribution is much narrower than the irradiance distribution. For $\lambda = 800$ nm and breakdown in water, it is narrower by a factor of $\sqrt{5} = 2.24$, which corresponds to a reduction of the affected volume by a factor of 11.2. The diameter of the free-electron distribution at the $1/e^2$ values amounts to 336 nm and the length to 806 nm.

It is interesting to note that the influence of the nonlinearity of the absorption process in plasma-mediated surgery considerably reduces the gain in spatial resolution that can be achieved by using a shorter wavelength. For example, when a wavelength of 355 nm is used instead of 800 nm, the width of the diffraction-limited irradiance distribution decreases by a factor of 2.25 but the plasma diameter decreases by a factor of only 1.42 because the order of the multiphoton process is reduced from 5 to 2 and the irradiance distribution is less strongly narrowed in the process of plasma formation. However, the irradiance range leading to low-density plasma formation is much broader for the shorter wavelengths (Fig. 5) thus making it easier to "tune" chemical and physical effects.

When the laser pulse energy is raised above the optical breakdown threshold, the spatial distribution of the free-electron density broadens because nonlinear absorption of laser light occurs upstream of the laser focus and limits the

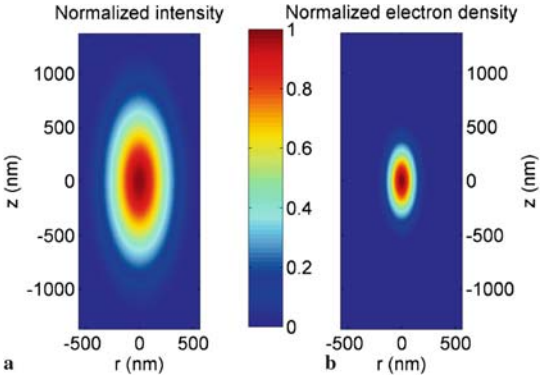

FIGURE 8 Normalized irradiance distribution (**a**) and electron-density distribution (**b**) in the focal region for NA = 1.3 and $\lambda = 800$ nm that are assumed for the numerical calculations of the temperature and stress evolution induced by femtosecond optical breakdown

possible energy density in the vicinity of the beam waist ('plasma shielding') [80, 126, 136–139]. Moreover, the $\varrho(I)$ dependence will strongly deviate from the proportionality to I^k when the critical electron density ϱ'_{cr} (3) is reached above which the plasma becomes highly reflective. Since the reflected light contributes to the plasma formation in the vicinity of the focus center, the electron-density distribution is flattened. The critical electron density ϱ'_{cr} for the change of the optical plasma properties amounts to $0.984 \times 10^{21}\,\mathrm{cm}^{-3}$ for $\lambda = 1064\,\mathrm{nm}$, to $3.94 \times 10^{21}\,\mathrm{cm}^{-3}$ for $\lambda = 532\,\mathrm{nm}$, and to $8.86 \times 10^{21}\,\mathrm{cm}^{-3}$ for 355 nm, respectively. We will see in Sect. 6.3 that the threshold for bubble formation is close to but still below these values. Therefore, the free-electron distribution depicted in Fig. 8 seems to be a reasonable approximation for the low-density plasma regime and suitable for the calculation of thermoelastic transients leading to bubble formation.

4 Chemical effects of low-density plasmas

Plasma-mediated chemical effects in biological media can be classified into two groups: 1. Changes of the water molecules by which reactive oxygen species (ROS) are created that affect organic molecules. 2. Direct changes of the organic molecules in resonant electron–molecule scattering.

1. The creation of ROS such as OH^* and H_2O_2 through various pathways following ionization and dissociation of water molecules has been investigated by Nikogosyan et al. [103] and recently reviewed by Garret et al. [143]. Both oxygen species are known to cause cell damage [144]. Heisterkamp et al. [16] confirmed the dissociation of water molecules during femtosecond-laser-induced plasma formation by chemical analysis of the gas content of the bubbles.

2. Capture of electrons into an antibonding molecular orbital can initiate fragmentation of biomolecules [143, 145–148], as shown in Fig. 9. Capture can occur when the electron possesses a 'resonant' energy for which there is sufficient overlap between the nuclear wave functions of the initial ground state and the final anion state. For a molecule XY this process corresponds to $e^- + XY \rightarrow XY^{*-}$, where the XY^{*-} has a repulsive potential along the X−Y bond coordinate. After a time of 10^{-15} to 10^{-11} s, the transient molecular anion state decays either by electron autodetachment leaving a vibrationally excited molecule (VE), or by dissociation along one or several specific bonds such as $XY^{*-} \rightarrow X^{\bullet} + Y^-$ (DA).

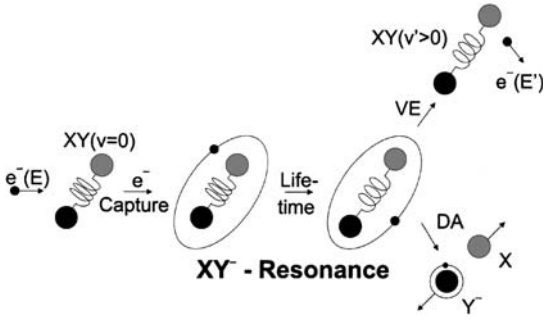

FIGURE 9 Dynamics of vibrational excitation and dissociative electron attachment in resonant electron–molecule scattering (see text). Reprinted with permission from Ref. [146]

Various authors describe resonant formation of DNA strand breaking induced by low-energy electrons (3–20 eV) [145, 147, 148]. Boudaiffa et al. [145] found that the maximum single-strand break (SSB) and double-strand break (DSB) yields per incident electron are roughly one or two orders of magnitude larger than those for 10–25-eV photons. It is conceivable that accumulative effects of this kind can lead to a dissociation/dissection of biological structures that are exposed to femtosecond-laser-generated low-density plasmas.

We will now assess the irradiance threshold for chemical changes by low-density plasmas using the plot of free-electron density vs irradiance presented in Fig. 3d. At NA = 1.3 and 800-nm wavelength, one free electron per focal volume corresponds to a density of $\varrho = 2.1 \times 10^{13}\,\mathrm{cm}^{-3}$. Our calculations yield the result that this value is reached at an irradiance of $I = 0.26 \times 10^{12}\,\mathrm{W\,cm}^{-2}$, which is 0.04 times the irradiance threshold for breakdown defined as $\varrho_c = \varrho_{cr} = 10^{21}\,\mathrm{cm}^{-3}$. Tirlapur et al. [144] experimentally observed membrane dysfunction and DNA strand breaks leading to apoptosis-like cell death after scanning irradiation of PtK2 cells with a peak irradiance of $I \approx 0.44 \times 10^{12}\,\mathrm{W\,cm}^{-2}$ in the focal region, or 0.067 times the calculated breakdown threshold. The observed damage pattern of membrane dysfunction and DNA strand breaks matches the effects expected from ROS and free electrons. The damage resembles the type of injury otherwise associated with single-photon absorption of UV radiation [144]. However, in Tirlapur's experiments it arose through nonlinear absorption of near-IR irradiation and the exposure of cells to low-density plasmas. The relative importance of effects from ROS and free electrons at large irradiances still needs to be investigated.

In some cases, the breaking of a single bond in polymeric biological structures induces a cascade of bond-breaking events that may be associated with a dramatic lowering of the apparent laser ablation threshold. For example, microtubules tagged with enhanced yellow fluorescent protein (EYFP) exhibit an exceptionally low threshold for laser-induced dissection with 76-MHz series of 532-nm, 80-ps pulses (0.01 nJ per pulse) [76], and an exceptionally low threshold was also observed for GFP-labeled microtubules irradiated by 80-MHz series of 880-nm, 100-fs pulses (0.025 nJ per pulse) [77]. The low dissection threshold seems to be related to the dynamic instability between growth and depolymerization that involves a rapid and self-propagating depolymerization of the 'open ends' after local breakage of the microtubules [149, 150]. Initiation of depolymerization requires breaking of just a single lateral bond, which could be induced either by the impact of free electrons in a low-density plasma or by multiphoton chemistry, enhanced by the EYFP or GFP labeling, respectively. Since they can be triggered by a single broken bond, these reactions differ from the usual fs laser ablation in the low-density plasma regime that arises as a cumulative effect of many bond-breaking events.

The irradiance producing lethal changes when laser pulse series are scanned over entire cells ($0.067 \times I_{rate}$) is slightly higher than the model prediction for the irradiance producing one free electron per pulse in the focal volume ($0.04 \times I_{rate}$), and about 10 free electrons in the focal volume will be produced by each laser pulse. Considering that the cell is exposed to thousands of pulses during the scanning irradiation,

cumulative chemical damage may arise from the free electrons. By contrast, when locally confined irradiation is used to achieve knockout of individual cell organelles or intracellular dissection, the irradiance threshold for cell death is considerably higher. The role of plasma-mediated chemical effects for these procedures will be discussed in Sect. 7.1, in comparison to the possible role of thermal and thermomechanical effects.

Recently, non-resonant ultra-fast processes of bond breaking induced by the large field strength in femtosecond laser pulses have been discussed in the context of laser ablation [151, 152]. However, these processes occur at surfaces where hot electrons can be emitted from the target, thus creating a large field among the remaining ions that can cause a Coulomb explosion, and where material decomposed by a strong laser field can freely expand. They are not likely to play a role in the bulk of transparent media, especially in the low-density plasma regime, i.e. at comparatively low field strengths. Here, chemical changes are rather generated through resonant interactions between quasi-free electrons and molecules.

5 Temperature evolution during pulse series

5.1 *Calculation of temperature distribution*

The deposition of laser energy into the medium is mediated by the generation and subsequent acceleration of free electrons. The energy carried by the free electrons is transferred to the heavy particles in the interaction volume through collisions and non-radiative recombination processes resulting in a heating of the atomic, molecular, and ionic plasma constituents. To assess the time needed to establish an equilibrium temperature, we need to look at the characteristic time for electron cooling (the transfer of kinetic electron energy during collisions) and at the time scale for recombination, which in water progresses through hydration of the free electrons. The time constant for electron cooling is of the order of only a few picoseconds [143, 153], and the time constant for hydration of free electrons in water is even shorter, about 300 fs [103]. However, the hydrated states possess a relatively long lifetime of up to 300 ns [103]. In the framework of our model, the different steps are treated as one recombination process according to (11). As the frequency of recombination events is proportional to ϱ_c^2, the recombination time depends on the free-electron density. It takes about 40 ps until the free-electron density decreases by one order of magnitude from a peak value of $\varrho_c = 10^{20}\,\mathrm{cm}^{-3}$, and about 20 ps for a peak value of $\varrho_c = 10^{21}\,\mathrm{cm}^{-3}$ [81, 91]. For low-density plasmas it will thus take between a few picoseconds and tens of picoseconds until a 'thermodynamic' temperature is established [143].

The temperature rise can be determined by calculating the volumetric energy density gained by the plasma during the laser pulse. This calculation is particularly easy for femtosecond pulses because the pulse duration is considerably shorter than the electron cooling and recombination times. Therefore, hardly any energy is transferred during the laser pulse, and the energy density deposited into the interaction volume is simply given by the total number density ϱ_{max} of the free electrons produced during the pulse multiplied by the mean energy gain of each electron. The mean energy gain of an electron is given by the sum of ionization potential $\tilde{\Delta}$ and average kinetic energy, the latter being $(5/4)\tilde{\Delta}$ for free electrons produced by cascade ionization (Sect. 2.2). This yields the following simple relation for the plasma energy density ε at the end of the laser pulse:

$$\varepsilon = \varrho_{max}(9/4)\tilde{\Delta}\,. \tag{18}$$

Note that this simple equation neglects the collisional energy transfer before impact ionization that is included in (8) and considered in more detail by more advanced models based on the use of complete collision integrals [21, 113]. This may lead to an underestimation of the rise in energy density corresponding to one free electron. On the other hand, (18) treats free electrons produced by multiphoton ionization in the same way as those produced by impact ionization even though they start with zero kinetic energy of electron and hole, which will rather overestimate the energy density increase. From (18), the temperature rise in the interaction volume after a single laser pulse can then be calculated by $\Delta T = \varepsilon/(\varrho_0 C_p)$, where C_p is the heat capacity and ϱ_0 the mass density of the medium.

The evolution of the temperature distribution within and around the interaction volume after a single 100-fs pulse ($\lambda = 800\,\mathrm{nm}$), during application of series of 100-fs pulses emitted at various repetition rates, and during cw laser irradiation ($\lambda = 514\,\mathrm{nm}$), was calculated by solving the differential equation for heat diffusion with the appropriate Green's function

$$\begin{aligned} T(x,y,z,t) = {} & \sum_{n=0}^{N-1} \int_0^{\min(t-n/f,\tau_L)} A \int_{-\infty}^{\infty}\int_{-\infty}^{\infty} \exp\left\{-2\left(\frac{x'^2+y'^2}{a^2}\right)-2\frac{z'^2}{b^2}\right\} \\ & \times \frac{1}{8\pi\varrho_0 C_p \kappa (t-n/f-t')} \\ & \times \exp\left\{\frac{(x-x')^2+(y-y')^2+(z-z')^2}{4\kappa(t-t')}\right\} \mathrm{d}x'\,\mathrm{d}y'\,\mathrm{d}z'\,\mathrm{d}t'\,. \end{aligned} \tag{19}$$

Here A is the peak density of absorbed power in the irradiated volume, f is the puls repetition rate, κ is the thermal diffusivity, a and b are the short and long half-axes of the free-electron-density distribution described by (17) ($1/\mathrm{e}^2$ values of electron density), $N = \mathrm{Int}(tf) + 1$ is the number of pulses which were absorbed until time t, and τ_L is the laser pulse width. The integrals over x', y', and z' were solved analytically using Mathematica software, whereas the integration over t' was done numerically. We assumed the temporal shape of the laser pulses to be rectangular. We used the values $\varrho = 1000\,\mathrm{kg\,m^{-3}}$ for the density, $C_p = 4187\,\mathrm{J\,K^{-1}\,kg^{-1}}$ for the heat capacity, and $\kappa = 1.38 \times 10^{-7}\,\mathrm{m^2\,s^{-1}}$ for the heat diffusivity of water [154].

5.2 *Evolution of the temperature distribution*

The spatial temperature distribution at the end of a single fs laser pulse, before heat diffusion sets in, reproduces the shape of the free-electron distribution of Fig. 8. Hence, the

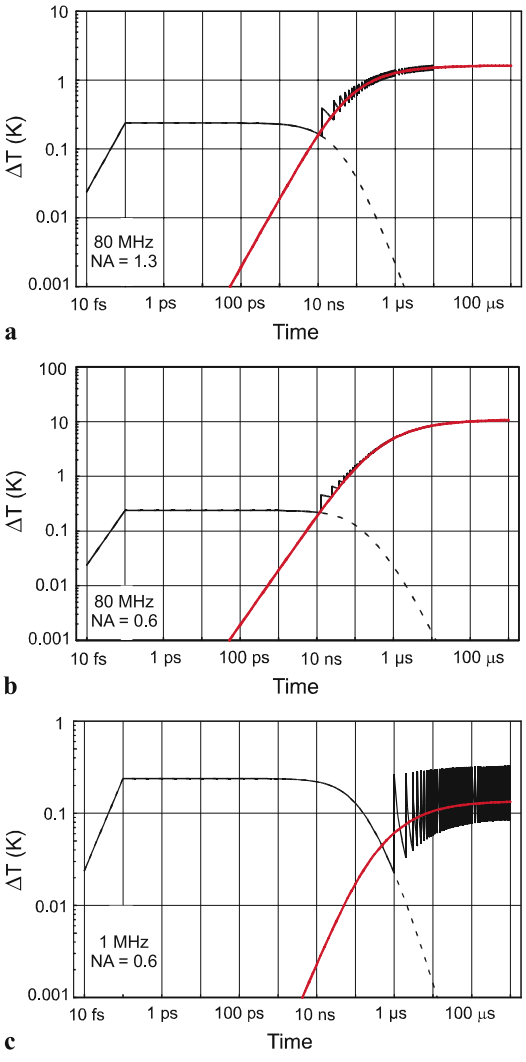

FIGURE 10 Temperature evolution at the center of the laser focus produced by a series of 800-nm, 100-fs pulses focused into water. (**a**) 80-MHz repetition rate, NA = 1.3; (**b**) 80-MHz repetition rate, NA = 0.6; (**c**) 1-MHz repetition rate, NA = 0.6. The volumetric energy density deposited per pulse is always $1\,\mathrm{J\,cm^{-3}}$ at the focus center. The *dashed lines* represent the temperature decay after a single pulse. For comparison, the temperature evolution during cw irradiation with the same average power as for the pulsed irradiation is also shown

diameter of the initial temperature distribution ($1/e^2$ values) amounts to 336 nm and the length to 806 nm (Sect. 3.2). Figure 10 shows the calculated temperature evolution at the center of the laser focus when series of 800-nm, 100-fs pulses are focused into water at different repetition rates (80 MHz and 1 MHz) and numerical apertures (NA = 1.3 and NA = 0.6). It was assumed that with each pulse an energy density of $1\,\mathrm{J\,cm^{-3}}$ at the center of the initial temperature distribution is deposited. For other values of the volumetric energy density, the shape of the temperature vs time curve will be the same but the absolute value of the temperature varies proportionally to the peak density of absorbed power, A. For comparison, we also calculated the temperature evolution during cw irradiation with the same average power as for the pulsed irradiation (dotted lines in Fig. 10a–c). For 80-MHz repetition rate, pulsed and continuous energy deposition differ significantly only during the first 100 ns.

The calculations in Fig. 10a for tightly focused irradiation with 80-MHz repetition rate reveal that the temperature is only 6.8 times larger after a few microseconds than the temperature increase caused by a single pulse. This implies that only a moderate heat accumulation occurs during plasma-mediated cell surgery. However, when the numerical aperture is reduced from NA = 1.3 to NA = 0.6, such as in Fig. 10b, a 45-fold temperature increase is predicted. Temperature accumulation can almost entirely be avoided if, at the same NA, the repetition rate is lowered to 1 MHz (Fig. 10c). In this case, the peak temperature in a long pulse series is only 1.36 times larger than after a single pulse. For 1-MHz repetition rate and NA = 1.3, this factor reduces to 1.024.

When laser surgery is performed with 80-MHz pulse series focused at NA = 1.3, the boiling temperature of 100 °C will, due to the 6.8-fold temperature accumulation, be reached when each individual pulse produces a temperature rise of 11.8 °C (starting from 20 °C room temperature). For 800-nm, 100-fs pulses this temperature rise requires a free-electron density of $\varrho_c = 2.1 \times 10^{19}\,\mathrm{cm^{-3}}$, which is reached at an irradiance of 0.51 times the value required for optical breakdown ($\varrho_{cr} = 10^{21}\,\mathrm{cm^{-3}}$).

The temperature distribution in the vicinity of the laser focus during application of 80-MHz pulse series is presented in Fig. 11 for different numerical apertures. The distribution arising from the ellipsoidal focus volume is plotted both in radial and axial directions. For NA = 1.3, the temperature distribution remains fairly narrow (FWHM $\approx$ 600 nm) even after a few milliseconds when a dynamic equilibrium between energy deposition and heat diffusion has been established. The rapid decrease of the temperature with increasing distance from the laser focus is related to the small size of the focal volume, which allows for rapid heat diffusion in all directions. By contrast, for NA = 0.6 the steady-state temperature distribution is more broadened compared to the single-pulse distribution, in addition to the stronger increase of the peak temperature. Both temperature accumulation and broadening of the temperature distribution can be avoided with repetition rates $\leq$ 1 MHz.

At first sight, the results of our temperature calculations might suggest that an irradiance range below the optical breakdown threshold exists where predominantly thermal effects in biological media can be produced. However, one needs to consider that about 10^6 free electrons per pulse are generated in the focal volume at the irradiance that creates a temperature difference of 11.8 °C per pulse and a peak temperature of 100 °C after a pulse series of several microseconds (for NA = 1.3). Any thermal denaturation of biomolecules will thus always be mixed with free-electron-induced chemical effects, and the latter will probably dominate.

5.3 *Comparison with cw irradiation of linear absorbers*

Since various researchers have produced cellular microeffects using long-pulsed or continuous-wave irradiation [47, 52, 56, 69–71], it is of interest to compare the widths of the temperature distributions produced by series of ultra-short laser pulses and cw irradiation.

Figure 12 shows the evolution of the temperature distribution when cw irradiation of 514-nm wavelength is fo-

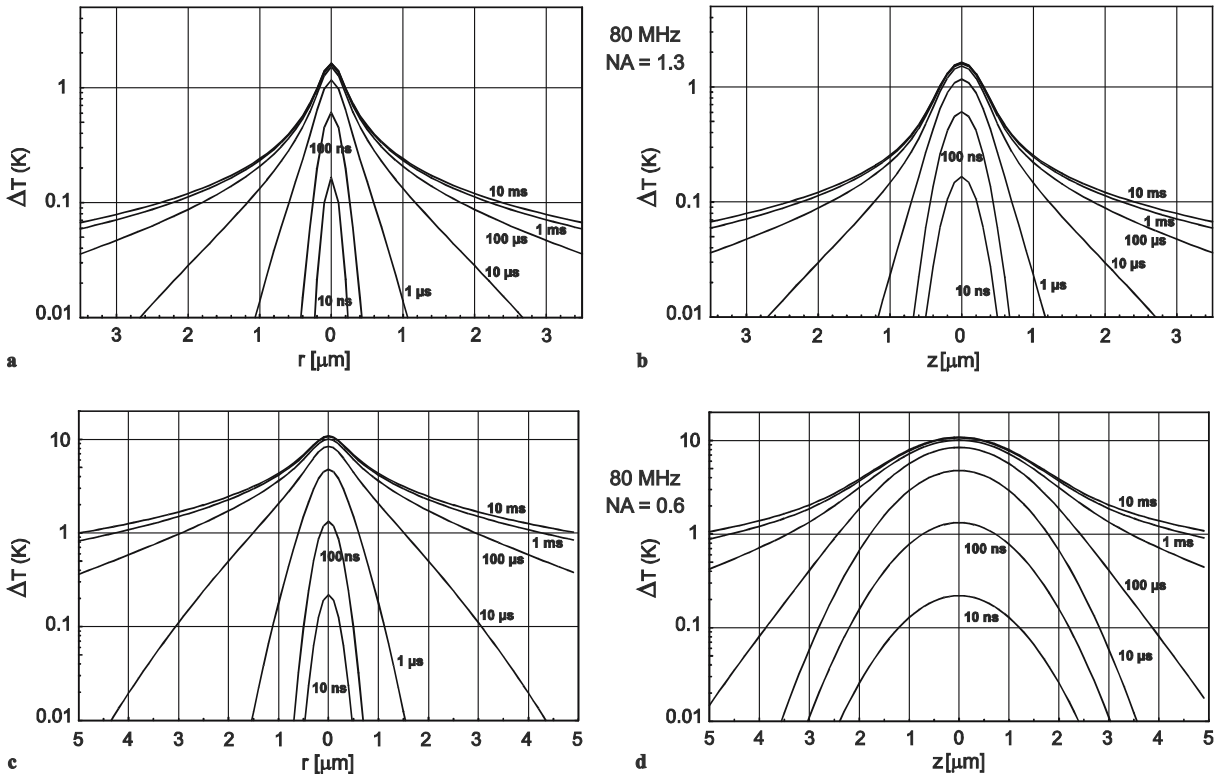

FIGURE 11 Temperature distribution in radial direction (**a**, **c**) and axial direction (**b**, **d**) produced by series of 800-nm, 100-fs pulses focused into water at numerical apertures of NA = 1.3 (**a**, **b**) and NA = 0.6 (**c**, **d**). The pulse-repetition rate was 80 MHz in both cases, and the volumetric energy density deposited at the focus center was 1 J cm^{-3} for each pulse

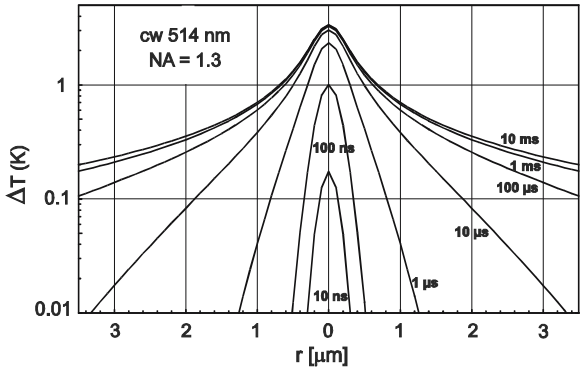

FIGURE 12 Evolution of the temperature distribution in radial direction produced by continuous energy deposition in a linearly absorbing aqueous medium at a laser wavelength of 514 nm. The calculations were performed for the same absorbed average power as in the case of pulsed, nonlinear energy deposition presented in Fig. 11

cused into a linearly absorbing aqueous medium at NA = 1.3. The temperature distribution is slightly broader (FWHM 850 nm) than that in Fig. 11a arising from nonlinear absorption of 80-MHz IR femtosecond pulse trains (FWHM 600 nm). The temperature distribution produced by femtosecond pulse trains is narrower because it originates from the free-electron distribution (18) rather than from the irradiance distribution (17) that is relevant for linear energy deposition. However, the spatial resolution of femtosecond laser surgery is not determined by the steady-state temperature distribution but by the width of the free-electron distribution itself, as we shall see in Sect. 7.1. Therefore, the spatial resolution of fs laser surgery is considerably better than that of a cw microbeam.

6 Thermoelastic stress generation and stress-induced bubble formation

6.1 *Calculation of stress distribution and bubble formation*

The temperature rise in the focal volume occurs during thermalization of the energy carried by the free electrons, i.e. within a few picoseconds to tens of picoseconds (see Sect. 5.1). This time interval is much shorter than the acoustic transit time from the center of the focus to its periphery. Therefore, no acoustic relaxation is possible during the thermalization time, and the thermoelastic stresses caused by the temperature rise stay confined in the focal volume, leading to a maximum pressure rise [2, 155, 156]. Conservation of momentum requires that the stress wave emitted from a finite volume within an extended medium must contain both compressive and tensile components such that the integral of the stress over time vanishes [155, 157]. The tensile stress wave may induce fracture of the material even after a temperature rise too small to produce thermal damage [158]. In water, it will cause the formation of a cavitation bubble when the tensile strength of the liquid is exceeded. For cell surgery, the threshold for bubble formation defines the onset of disruptive mechanisms contributing to dissection.

To determine the evolution of the thermoelastic stress distribution in the vicinity of the laser focus, we solved the three-dimensional thermoelastic wave equation. A starting point for

the calculation of the thermoelastic stress wave propagation is the temperature distribution at the end of a single femtosecond laser pulse that reproduces the free-electron distribution described by (17). In the following calculations, this temperature distribution is characterized by $T_{\max}$, the temperature in °C in the center of the focal volume. From this temperature distribution the initial thermoelastic pressure (right after the laser pulse, before the acoustic wave has started to propagate) was calculated using

$$p(\boldsymbol{r}) = \int_{T_1}^{T_2(\boldsymbol{r})} \frac{\beta(T)}{K(T)}\,\mathrm{d}T\,, \tag{20}$$

where $T_1 = 20\,^{\circ}\mathrm{C}$ is the temperature before the laser pulse, and $T_2(\boldsymbol{r})$ the temperature of the plasma after the laser pulse, which depends on the location within the focal volume. The temperature dependence of the thermal expansion coefficient β and the compressibility K was taken into account, using values for metastable water from [159]. The time- and space-dependent pressure distribution $p(\boldsymbol{r}, t)$ due to the relaxation of the initial thermoelastic pressure was calculated using a k-space (spatial frequency) domain propagation model [160, 161].

Because the heated volume is very small ($\approx 0.07\,\mu\mathrm{m}^3$) and the region subjected to large tensile stress amplitudes is even smaller (see Fig. 14, below), the presence of inhomogeneous nuclei that could facilitate bubble formation is unlikely. Therefore, we have to consider the tensile strength of pure water to estimate the bubble-formation threshold in femtosecond optical breakdown. Traditionally, the rupture of a liquid achieved by tensile stress under isothermal conditions is called 'cavitation' while bubble formation due to heating under isobaric conditions is called 'boiling' [162]. Such a distinction becomes obscure when targets are both heated and stretched under conditions of stress confinement. We use the crossing of the 'kinetic spinodal' as defined by Kiselev [163, 164] as threshold criterion for bubble formation. In the thermodynamic theory of phase transitions, the locus of states of infinite compressibility $(\partial p/\partial V)_{\mathrm{T}} = 0$, the spinodal, is considered as a boundary of fluid metastable (superheated) states. Physically, however, the metastable state becomes short-lived due to statistical fluctuations well before the spinodal is reached [159, 165]. The kinetic spinodal is the locus in the phase diagram where the lifetime of metastable states becomes shorter than a relaxation time to local equilibrium. If the surface tension is known, the physical boundary of metastable states in this approach is completely determined by the equation of state only, i.e. by the equilibrium properties of the system [163, 164]. This feature distinguishes the kinetic spinodal from the homogeneous nucleation limit derived earlier by Fisher, which depends on the size of the volume under consideration and the duration of the applied stress [166]. Unlike Fisher's equation, the kinetic spinodal reproduces the shape of the spinodal and is applicable in the entire temperature range from room temperature to the critical point. The nucleation thresholds in cells will probably resemble those in pure water because the biomolecules are too small to serve as boundaries for heterogeneous nucleation.

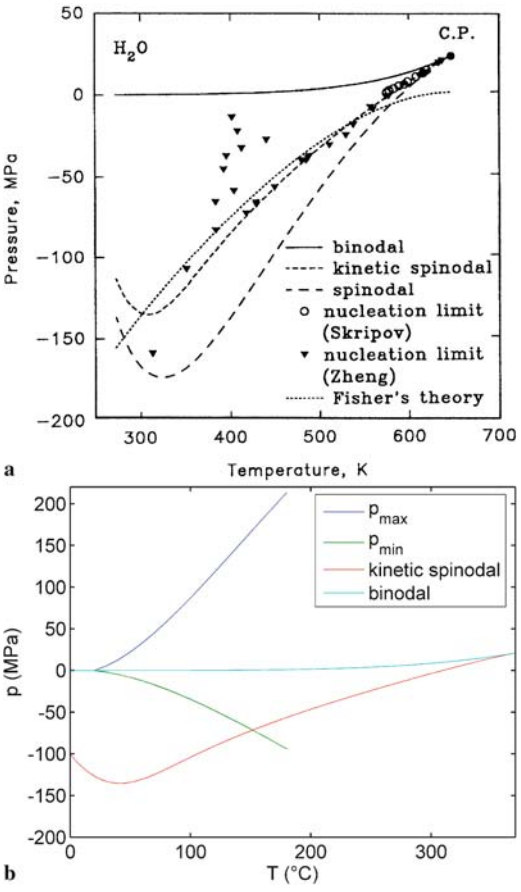

FIGURE 13 (**a**) Binodal, spinodal, and kinetic spinodal of water as a function of temperature, calculated with the analytic equation of state of Saul and Wagner [240]. The *dotted curve* corresponds to the homogeneous nucleation limit in Fisher's theory [166], the *circles* indicate experimental data of Skripov et al. [159], and the *triangles* indicate the experimental data of Zheng et al. [167] recalculated in p–T coordinates. Figure reproduced with permission from Ref. [163]. Copyright 1999 Elsevier Science B.V. (**b**) Peak compressive and tensile thermoelastic stresses in the focus center produced by a 800-nm, 100-fs pulse focused into water at NA = 1.3, plotted together with the binodal and the kinetic spinodal

Figure 13a presents the saturated liquid/vapor curve (binodal), the spinodal, the kinetic spinodal, and the homogeneous nucleation limit derived by Fisher in a p vs T projection of the thermodynamic phase diagram for water. For comparison, experimental data by Skripov et al. on the empirical limit of the metastable region and by Zheng et al. on the tensile strength of water are also shown [159, 167]. In Fig. 13b, the kinetic spinodal is plotted together with the peak compressive and tensile thermoelastic stresses in the focus center that are produced when an 800-nm, 100-fs pulse is focused into water at NA = 1.3. The temperature at which the tensile stress curve reaches the kinetic spinodal is defined as the bubble-formation threshold. For larger laser pulse energies, the kinetic spinodal will be reached in an increasingly large part of the focal region.

To calculate the dynamics of the cavitation bubble produced after crossing the kinetic spinodal, first the size of the bubble nucleus was determined. It was identified with the extent of the region in which the negative pressure exceeds the kinetic spinodal limit $p(\boldsymbol{r}, t) < p_{\mathrm{ks}}(\boldsymbol{r})$. The initial radius of a spherical bubble with the same volume was taken

as the starting nucleus for the cavitation bubble. The heated and stretched material within the nucleus commences to expand instantaneously (within less than 1 ps) once the kinetic spinodal is reached [168]. As driving force for the expansion only the negative part of the time-dependent stress in the center of the focal volume was considered, because the nucleus does not exist before the tensile stress arrives. This is in contrast to simulations of heterogeneous cavitation where pre-existing gas bubbles interact with a time-varying pressure wave [158]. Only cases were simulated in which the temperature in the center of the focal volume slightly exceeds the phase-transition threshold and the size of the resulting nucleus is small compared with the focal volume. This justifies using the tensile stress amplitude in the center of the undisturbed focal volume as driving force for the bubble expansion. For larger laser pulse energies one would need to consider that the tensile stress is diminished by the rupture of the liquid.

After the passage of the tensile stress transient, the vapor pressure p_v inside the bubble continues to drive the bubble expansion. The initial vapor pressure is calculated for a temperature averaged over all volume elements within the nucleus. During bubble growth, it will drop due to the cooling of the expanding bubble content. This cooling is counteracted by heat diffusion from the liquid surrounding the bubble. The temperature of this liquid, on the other hand, drops because of heat diffusion out of the focal volume as depicted by the dashed lines in Fig. 10. To quantify the temporal evolution of the driving pressure, we consider two limiting cases:

Case 1: Bubble size $\ll$ focal volume. We assume that the bubble initially expands adiabatically until the average temperature of the bubble content has fallen to the temperature of the liquid at the nucleus wall. Afterwards, heat flow from the surrounding liquid maintains the temperature of the bubble content at the same level as that of the surrounding liquid. The bubble pressure $p_v(t)$ thus equals the equilibrium vapor pressure corresponding to the temperature at the nucleus wall, which, for NA = 1.3, decays within about 20 ns to 1/e of its initial value (Fig. 10a). Justifications for this hypothesis are the small bubble size and the fact that the bubble nucleus is not empty but contains material that is initially at liquid density and has a relatively large heat capacity.

Case 2: Bubble size comparable to or larger than the focal volume. When the size of the nucleus becomes comparable to the size of the focal volume, the bubble expands more rapidly. In this case, the heated liquid shell surrounding the bubble is rapidly thinned, which leads to an accelerated heat dissipation into adjacent liquid. The heat flow into the bubble is probably small compared with the amount of heat contained in the material within the bubble nucleus. Therefore, the entire bubble dynamics is modeled as an adiabatic expansion. As a consequence, the vapor pressure drops much faster than in case 1. In both cases, the ongoing phase transition in the bubble was neglected to obtain tractable expressions for $p_v(t)$. This simplification enabled us to use the Gilmore model to describe the bubble dynamics [158, 169, 170]. The pressure drop is in case 1 slower and in case 2 faster than the pressure decay corresponding to the actual phase transitions of the bubble content. Therefore, these cases represent upper and lower limits for the evolution of the actual bubble size after femtosecond optical breakdown.

6.2 *Evolution of the stress distribution*

The thermalization time of the energy carried by the free electrons was assumed to be 10 ps. For NA = 1.3, $\lambda = 800$ nm, and a sound velocity in water of $c_0 = 1500$ m/s, the acoustic transit time to the periphery of the heated region with 168-nm radius is 112 ps. Thus, the dimensionless thermalization time (thermalization time divided by acoustic relaxation time) is $t_p^* = 0.09$, which corresponds to a very high degree of stress confinement. The 'thermalization pulse' was assumed to have a Gaussian temporal shape, with the peak at $t = 0$. By comparison with an exponential thermalization pulse we found that, for short dimensionless pulse durations t_p^*, the pulse shape has little influence on the shape and amplitude of the stress wave.

Figure 14 shows the spatial stress distribution in radial and axial directions for various points in time after the release of the laser pulse, and Fig. 15 presents the temporal evolution of the stress amplitude in the center of the focal volume. All pressure amplitudes are normalized to the peak compressive stress created in the focal volume.

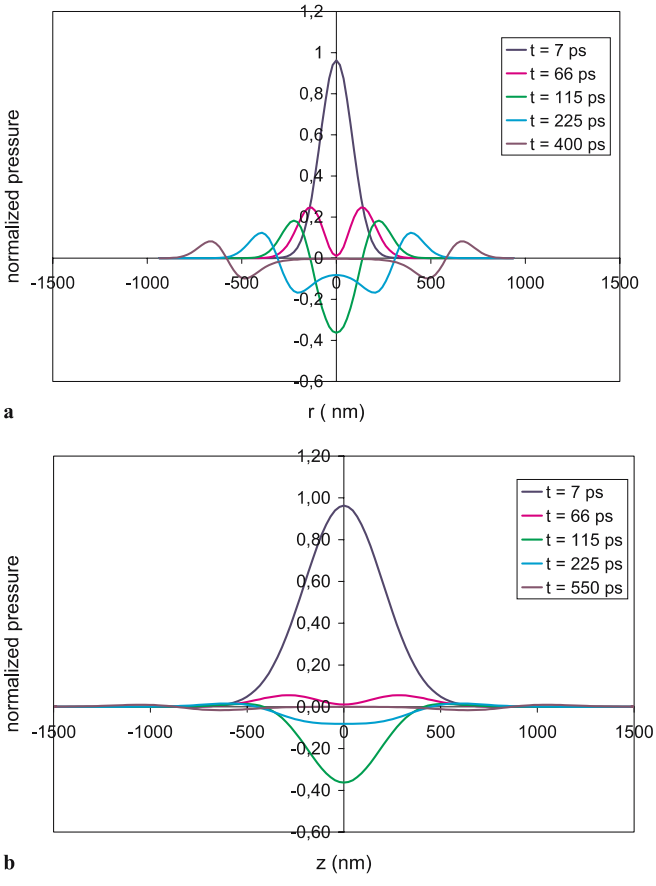

FIGURE 14 Stress distribution produced by a single femtosecond pulse of 800-nm wavelength focused into water (NA = 1.3), for various times after the release of the laser pulse; (**a**) in radial direction, (**b**) in axial direction. The thermalization time of the energy carried by the free electrons was assumed to be 10 ps. The dimensionless thermalization time (thermalization time divided by acoustic relaxation time) was $t_p^* = 0.09$. The 'thermalization pulse' was assumed to have a Gaussian temporal shape, with the peak at $t = 0$. The pressure amplitudes are normalized to the peak compressive stress created in the focal volume

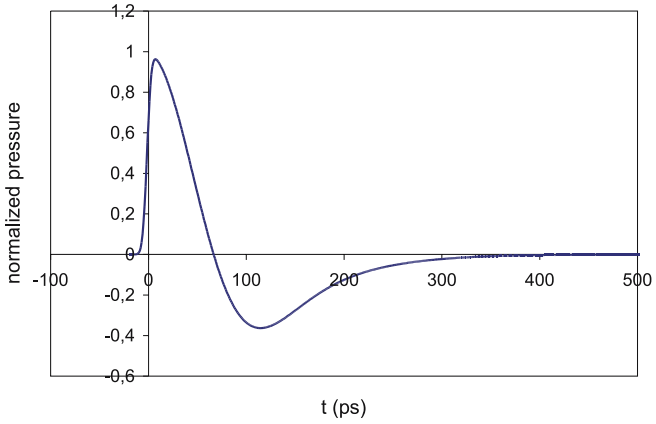

FIGURE 15 Temporal evolution of the stress amplitude in the center of the focal volume for the same conditions as in Fig. 14

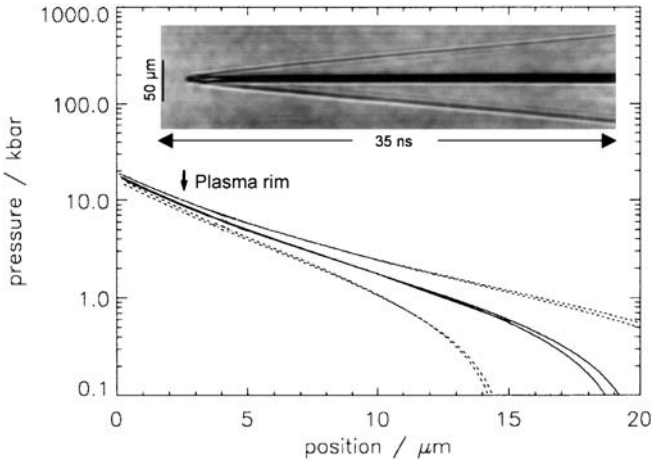

FIGURE 16 Measured pressure vs propagation-distance curve for a stress wave produced by a 100-fs pulse of 5-μJ energy ($E/E_{th} = 30$) focused into distilled water at NA = 0.2 (16° full focusing angle). The laser wavelength was 580 nm. The *arrow* represents the location of the plasma rim as determined from plasma photographs in side view. The $p(d)$ curve was determined from the streak recording of the stress-wave emission shown in the *inset*

The compressive stress generates a stress wave traveling into the surrounding medium. When the thermal expansion comes to a rest, inertial forces lead to the generation of a relaxation wave that propagates from the periphery of the focal volume towards its center and is focused in the center of symmetry. Because of the geometrical focusing, it turns into a tensile stress wave that achieves maximum amplitude at the center of symmetry.

The peak tensile stress amplitude depends strongly on the shape of the heated volume. It is largest for a spherical shape [155] and much smaller in the present case of an elongated ellipsoid. The dependence of the compressive stress amplitude on the degree of stress confinement t_p^* was relatively strong, but the amplitude of tensile stress waves remained approximately constant when the duration of the thermalization pulse was varied between 5 ps, 10 ps, and 20 ps.

A comparison of Fig. 14a and b shows that the stress-wave amplitudes outside the focal region are considerably larger in the radial than in the axial direction. This is a consequence of the elongated shape of the focal volume. The stress transients emitted in both directions have a bipolar shape as expected for thermoelastic waves. The amplitude of the stress transient when it leaves the heated region in the radial direction amounts to 25% of the peak compressive pressure. This differs from the previously analyzed case of a top-hat distribution, where the amplitude of the compressive wave just outside the heated volume amounts to 0.5 times the peak compressive pressure inside that volume [97].

Experimental data on stress-wave emission. Measurements of the stress waves produced by femtosecond optical breakdown at large NA and close to the breakdown threshold are very challenging because of the sub-micrometer size of the breakdown volume and the sub-nanosecond duration of the stress transients (Figs. 14 and 15). Hydrophones with sufficiently small detector size to resolve the shape of the transient close to their source are not available, and optical techniques [96, 171–173] also do not provide the necessary spatial resolution. Therefore, we performed measurements at smaller numerical aperture (NA = 0.2) to assess the stress amplitudes arising during femtosecond optical breakdown.

Investigations for irradiances well above the breakdown threshold were done by means of streak photography and subsequent digital image analysis of the streak recordings [127, 128, 173]. Differentiation of the stress wave propagation curves $r(t)$ obtained from the streak recordings yielded the stress-wave velocity that is related to the pressure amplitude by the known Rankine–Hugoniot relationship for water [174] if the stress wave has shock-wave properties. The analysis yielded the entire pressure vs distance curve in the immediate vicinity of the breakdown region perpendicular to the optical axis as shown in Fig. 16.

The determination of the shock-wave pressure becomes inaccurate for pressure amplitudes below 100 MPa, where the deviation of the propagation velocity from the sonic velocity becomes too small to be measured accurately with the streak technique [173]. Therefore, the streak technique could only be applied for shock-wave measurements at energies 15–150 times above the breakdown threshold. Stress-wave amplitudes closer to the optical breakdown threshold were determined indirectly by hydrophone measurements at 6-mm distance from the focus [127] and extrapolation of these data to the plasma rim. We used a PVDF hydrophone (Ceram) with a rise time of 12 ns, an active area of 1 mm^2, and a sensitivity of 280 mV/MPa (calibrated by the manufacturer up to a frequency of 10 MHz). A distance of 6 mm between detector and laser focus was required to avoid measurement errors arising from the intersection of a spherical shock wave with a plane detector [96]. Measurement results for energies from close to the breakdown threshold up to 80 times threshold are shown in Fig. 17.

The results of far-field hydrophone measurements can be extrapolated to the boundary of the focal region if the decay constant n of the pressure decay $p \propto r^n$ with increasing propagation distance r is known. The decay constant was estimated by comparing pressure values at the plasma rim and in the far field that were measured at larger laser pulse energies. For example, for $E = 30 \times E_{th}$, the pressure at the plasma rim ($r = 2.2$ μm) is 900 MPa (Fig. 16), and the pressure measured

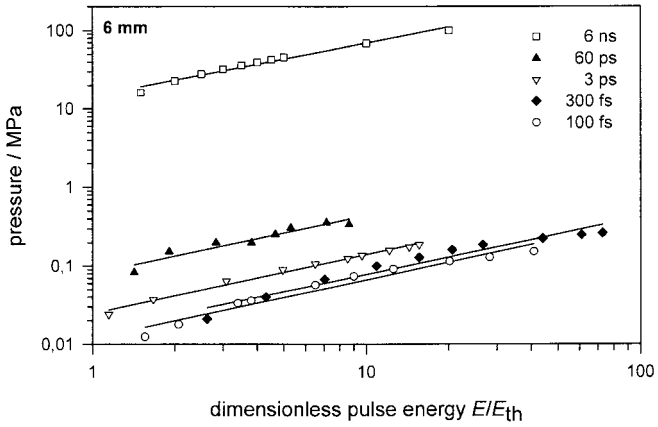

FIGURE 17 Stress-wave amplitude for 100-fs pulses and longer pulse durations as a function of the dimensionless laser pulse energy E/E_{th}. The pressure amplitudes were measured by means of a hydrophone at 6-mm distance from the laser focus

at 6-mm distance is 0.12 MPa (Fig. 17). The resulting decay constant is $n = 1.13$. Previous investigations of complete $p(r)$ curves for spherical shock waves produced by 30-ps pulses of 50-μJ energy yielded a very similar constant of $n = 1.12$ over a large range of propagation distances [96].

An estimate of the pressure value at 6-mm distance produced by a 100-fs pulse with threshold energy was obtained by extrapolating the data for $E/E_{th} \geq 1.5$ in Fig. 17 to $E = E_{th}$. It is about 0.008 MPa. The plasma radius at E_{th} was identified with the focal radius of 2.2 μm measured using a knife-edge technique [127]. A pressure of $p = 0.008$ MPa at 6-mm distance corresponds to a pressure value of 61 MPa at the plasma rim when a decay constant $n = 1.13$ is assumed, and to a value of 56 MPa with a decay constant of $n = 1.12$, respectively. Our calculations of the thermoelastic stress generation predict a peak pressure of 168 MPa at the bubble-formation threshold (see Sect. 6.3, below). According to Fig. 14, the stress transient that leaves the heated region in the radial direction has a peak pressure of $\approx 25\%$ of the maximum compressive amplitude within the focal volume. We thus obtain a theoretical prediction of 42 MPa for the amplitude of the thermoelastic stress wave at the plasma rim. Considering the uncertainties in the location of the plasma rim and the differences in numerical aperture between experiment and calculation, the agreement between experimental results (56–61 MPa) and calculated data (42 MPa) is very good.

Both experiments and calculations reveal that stress confinement in femtosecond optical breakdown results in the generation of high pressure values even though the temperature rise is only relatively small. In a purely thermal process, a temperature rise to, for example, 200 °C starting from room temperature would produce a saturation vapor pressure of 1.6 MPa. The compressive pressure transient produced by a temperature rise of 180°C under stress-confinement conditions has an amplitude of 220 MPa, which is more than two orders of magnitude larger than the vapor pressure.

The situation is different for optical breakdown at longer pulse durations where the stress-confinement condition is not fulfilled. Here, high pressures are always associated with high temperatures and plasma energy densities. For pulses which are considerably longer than the thermalization time of the free-electron energy, a dynamic equilibrium between generation of free electrons and thermalization of their energy is established during the laser pulse [81]. This leads to a high value of the plasma energy density [80] and a temperature of several thousand degrees Kelvin [175–177]. The duration of the resulting shock wave is determined by the time it takes for the high pressure within the plasma to decrease during the plasma expansion [96], which for NA = 0.9 was found to be about 25–40 ns [3]. By contrast, the duration of the thermoelastic stress transients is determined by the geometric dimensions of the breakdown volume, which are in the sub-micrometer range. This leads to a duration of the stress transients of the order of or less than 300 ps (Fig. 15). The short duration of these stress waves is correlated with a small energy content (see also Sect. 6.4).

6.3 *Threshold for stress-induced bubble formation*

A specific feature of the stress transients generated during fs optical breakdown is their tensile component that is related to the high degree of stress confinement during energy deposition. The tensile stress makes it possible that a cavitation bubble can be generated by a relatively small temperature rise in the liquid. The threshold for bubble formation is defined by the temperature rise leading to a crossing of the kinetic spinodal, as shown in Fig. 13. For $\lambda = 800$ nm, NA = 1.3, and a room temperature of 20 °C, the critical temperature rise and the corresponding critical tensile stress are $\Delta T = 131.5$ °C and $p = -71.5$ MPa, respectively. The corresponding compressive pressure is 168 MPa.

The temperature rise of 131.5 °C at the threshold for bubble formation corresponds to an increase in energy density of 551 J cm^{-3} which, according to (18), is produced by a free-electron density of $\varrho_c = 0.236 \times 10^{21}$ cm^{-3}. This electron density is less than the breakdown criterion of $\varrho_{cr} = 10^{21}$ cm^{-3} assumed in our numerical calculations and in most other theoretical studies of plasma formation. The discrepancy between the threshold values relying on different breakdown criteria needs to be kept in mind when comparing the results of experimental studies, where bubble formation serves as breakdown criterion, with those of numerical simulations.

The fact that femtosecond optical breakdown is associated with only a relatively small temperature rise explains why plasma luminescence is no longer visible for pulse durations shorter than about 10 ps [122, 128]. For pulse durations longer than the thermalization time, large amounts of energy are transferred from the free electrons to the heavy particles during the laser pulse [81], resulting in a temperature of several thousand degrees Kelvin, bubble formation, and a bright plasma luminescence [175–177]. By contrast, a peak temperature of 151.5 °C reached at the threshold for bubble formation with 100-fs pulses is too low to produce black-body radiation in the visible range of the optical spectrum. Moreover, the recombination radiation of femtosecond-laser-produced plasmas is weak because only one 'set' of free electrons is produced that recombines after the end of the laser pulse. The energy density will remain small also at energies above the threshold for bubble formation because of the shielding of the focal region by plasma formation upstream of the focus [80, 126, 136–139] (see Sect. 3.2). Therefore, bubble formation is

Pulse duration	Wavelength (nm)	NA or focusing angle	Gaussian (G) Top hat (T)	Measured spot diameter (μm)	Diffraction-limited spot (μm)	Breakdown criterion Bubble (B) Luminescence (L)	E_{th} (μJ)	F_{th} (J/cm^2)	I_{th} $\times 10^{11}$ (W/cm^2)	I_{rate} $\times 10^{11}$ (W/cm^2)	Source	Factors influencing the measured threshold value
10 ns	1064	14°	G		4.0	L	400	3200	3.2		[178]	Spherical aberrations, ps spikes because of longitudinal mode beating
7 ns	1064		G		75	L		245	0.35		[99, 100]	Longitudinal mode beating, self-focusing
6 ns	1064	32°	G	5.4		L	89.9	396	0.66	1.79	[15]	Longitudinal mode beating
6 ns	532	22°	G	5.3		L	38.5	174	0.29	6.06	[15]	Longitudinal mode beating
6 ns	1064	NA 0.9	T		1.44	L	18.3	1122	1.87		[3]	Longitudinal mode beating, absorption in microscope objective not considered
6 ns	532	NA 0.9	T		0.72	L	1.89	462	0.77		[3]	Longitudinal mode beating; absorption in microscope objective not considered
220 ps	1064		G		37	L		64.9	2.95	1.81 (100 ps)	[99, 100]	Self-focusing
200 ps	800	NA 0.65	T		1.50	B	4.0	90.4	4.52	2.90 (100 ps)	[179, 180]	Spherical aberrations
60 ps	532	16.7°	T	7.2		L	10.0	24.4	4.07	6.63 (100 ps)	[136]	Moderate spher. aberrations
40 ps	1064	14°	G		4.0	B	1.6	64.0	16		[178]	Spherical aberrations
30 ps	1064		G		37	L		19.2	6.41		[99, 100]	Self-focusing
30 ps	1064	22°	G	4.7		L	2.38	13.6	4.53	2.67 (10 ps)	[15]	
30 ps	532	22°	G	3.4		L	1.01	11.3	3.75	6.19 (10 ps)	[15]	
3 ps	580	16.7°	TG	10.8		B	1.1	1.25	4.15		[136]	Moderate spher. aberrations
3 ps	580	16°	G	5.0		B	0.51	2.6	8.5	15.3 (1 ps, 532 nm)	[80, 81]	
300 fs	580	16.7°	TG	10.8		B	1.0	1.1	36.0		[136]	Moderate spher. aberrations, self-focusing
300 fs	580	16°	G	5.0		B	0.29	1.4	47.6		[15]	Self-focusing
150 fs	620			5.0		B		0.87	58.0		[181]	Self-focusing
150 fs	620			5.0		B		1.3	86.7		[181]	Self-focusing
125 fs	580	16.7°	TG	10.8		B	0.35	0.4	30.6		[136]	Moderate spher. aberrations, self-focusing
100 fs	580	16°	G	4.4		B	0.17	1.1	111.0	55.9 (532 nm)	[80, 81]	Self-focusing
100 fs	800	NA 0.65	T		1.50	B	≈ 0.1	5.64	564	65.4	[182]	Spherical aberrations
44 fs	810	$\approx 16°$	G	≈ 10		B	0.19	0.22	50		[183]	Strong self-focusing

TABLE 1 Experimental optical breakdown thresholds for water, together with calculated threshold values obtained using the criterion $\varrho_{cr} = 10^{21}$ cm^{-3}. Whenever the spot size was determined in the experiment, the measured spot size is quoted and used for the threshold calculations. Measured spot sizes refer to the 'linear' size, without the influence of self-focusing. When the spot diameter was not measured, the diffraction-limited spot size is quoted and used for calculating the thresholds. Spot sizes refer to the $1/e^2$ values of the intensity for irradiation with a Gaussian beam profile, and to the first minimum of the Airy function for irradiation with a top-hat beam profile. Factors compromising the accuracy of the measured threshold data are listed in the *column on the far right* of the table

a more useful breakdown criterion for ultra-short laser pulses than plasma luminescence.

Experimental data on breakdown thresholds. A comparison between experimental threshold data from various researchers and threshold values predicted by our model is presented in Table 1. Note that calculated values refer to the peak power in the laser pulse and in the focal spot while experimental data are often calculated using the average power in the laser pulse and within the focal area.

Our numerical predictions lie within the range of experimental data for all pulse durations. However, that does not mean very much considering the fact that the experimental data scatter within a range of one order of magnitude for femtosecond and nanosecond pulses, and only slightly less for picosecond pulses. These large variations reflect the difficulty of performing precise threshold measurements in the bulk of water. Ideally, high-quality laser beams and diffraction-limited focusing optics should be employed, the spot size should be measured to control the beam quality, and I_{th} should be calcu-

lated using the measured spot size. However, in various studies, the quality of the laser beam and focusing optics were far from optimal and, nevertheless, the diffraction-limited spot size has been used for the calculation of I_{th}. In the presence of aberrations, this leads to erroneously large threshold values. Even when the spot size is measured, aberrations will lead to false results because breakdown occurs in hot spots within the focal region that are smaller than the measured spot size. The threshold values determined in this way are, therefore, smaller than the actual values [184]. Many breakdown experiments were performed by focusing a laser beam into a glass cell by means of external focusing optics. Even when this optics is of high quality, the glass cell itself will introduce spherical aberrations. This source of error can be avoided by using water-immersion microscope objectives built into the wall of the cell [3].

For nanosecond pulses, longitudinal mode beating in the laser resonator will usually produce intensity spikes of picosecond duration with amplitudes up to 4–5 times as large as the averaged intensity. Such statistical fluctuations of the peak irradiance are a major cause of the wide statistical distribution of optical breakdown thresholds and substantially reduce their absolute values [185, 186]. Therefore, single-frequency lasers providing a temporally Gaussian pulse shape should be used for threshold measurements. However, to date all measurements of nanosecond optical breakdown thresholds in water have been performed with longitudinally multimode laser beams.

To avoid a change of the focal spot size by nonlinear beam propagation, sufficiently large focusing angles must be used [5, 15, 187]. While this is easy to achieve for nanosecond pulses, a numerical aperture NA ≥ 0.9 is required for a pulse duration of 100 fs to be sure to exclude a diminution of the spot size by self-focusing and the corresponding apparent reduction of the breakdown threshold [5]. To date, no threshold data obtained with such large NAs are available for ultra-short laser-induced breakdown in water. We must conclude that the present experimental data basis is not reliable enough to perform a thorough comparison with theoretical predictions. Future measurements with aberration-free temporally Gaussian laser pulses focused at large NA will have to fill this gap.

In addition, a better adjustment of the numerical breakdown criterion to the experimental criterion of bubble formation is needed to enable a meaningful comparison of experimental data with model predictions. While bubble formation requires an approximately constant energy density within the focal volume for all laser pulse durations and wavelengths, the energy density associated with a fixed value of the free-electron density, such as $\varrho_{cr} = 10^{21}$ cm^{-3}, varies considerably with pulse duration. Thus, the assumption of a constant free-electron density as breakdown criterion is quite arbitrary, especially for cases where the threshold is smooth, i.e. where ϱ_{max} increases continuously with irradiance. In these cases it seems more reasonable to relate the critical free-electron density to the energy density within the medium that leads to bubble formation. Equation (17) provides the required link between electron and energy densities, and an analysis of $\varrho_{max}(I/I_{rate})$ curves (Figs. 3 and 5) then yields the corresponding threshold irradiance.

The new threshold definition for the numerical model will yield a better match between the experimentally observed and numerically predicted wavelength dependence of breakdown thresholds than the values in Table 1. Experimentally, the thresholds for ns and ps pulses decrease with decreasing wavelength [3, 15], but values calculated with a constant ϱ_{cr} show the opposite trend. Previous calculations revealed a relatively smooth threshold for ns and ps breakdown with visible and UV wavelengths, in contrast to the sharp threshold for IR wavelengths shown in Fig. 3c [91]. Calculated threshold values based on the new definition will for IR wavelengths thus be the same as those obtained with $\varrho_{cr} = 10^{21}$ cm^{-3}, but they will be lower for visible and UV wavelengths, in accord with experimental observations.

6.4 *Cavitation bubble dynamics*

Figure 18 shows a two-dimensional representation of the evolution of the thermoelastic stress wave and of the region in which the kinetic spinodal is surpassed (bubble nucleus) for a peak temperature of 200 °C, slightly above the threshold for bubble formation. The subsequent bubble dynamics calculated for cases 1 and 2 described in Sect. 6.1 is presented in Fig. 19. It turned out that for a vapor pressure that changes adiabatically with bubble size (case 2 in Fig. 19b) the bubble motion is very similar to the case where the vapor pressure is not taken into account at all and only the negative-pressure pulse drives the bubble expansion (not shown). Figure 20 shows the maximum bubble radii for case 1 and case 2 as a function of the maximum temperature achieved in the center of the focal volume, together with the radius of the nucleus, R_0. Close to threshold, the actual bubble radius will probably resemble case 1 in which the bubble nucleus is assumed to be much smaller than the focal region. For energies well above threshold, the predictions obtained for case 2 become more realistic.

The most prominent feature of the transient bubbles produced close to the threshold of femtosecond optical breakdown is their small size and short lifetime. The bubble radius amounts to only about 200 nm in water, and will be even smaller in a visco-elastic medium such as the cytoplasm. This makes a dissection mechanism associated with bubble formation compatible with intracellular nanosurgery, in contrast to nanosecond optical breakdown ($\tau_L = 6$ ns, $\lambda = 1064$ nm) where the smallest bubble radius in water observed for NA $= 0.9$ was $R_{max} = 45$ μm [3]. The small bubble size corresponds to a small energy,

$$E_B = \frac{4\pi}{3}(p_\infty - p_v)R_{max}^3 , \tag{21}$$

of the expanded bubble. For the case presented in Fig. 19a, it amounts to 5.3×10^{-15} J (5.3 femtojoules). The smallness of the bubble energy is largely due to the small energy content of the stress transient creating the bubble. This energy is equal to the energy stored in thermoelastic compression of the heated fluid volume [156],

$$E_{TE} = \frac{1}{2\varrho_0 c_0^2}\int p_0^2 \, \mathrm{d}V , \tag{22}$$

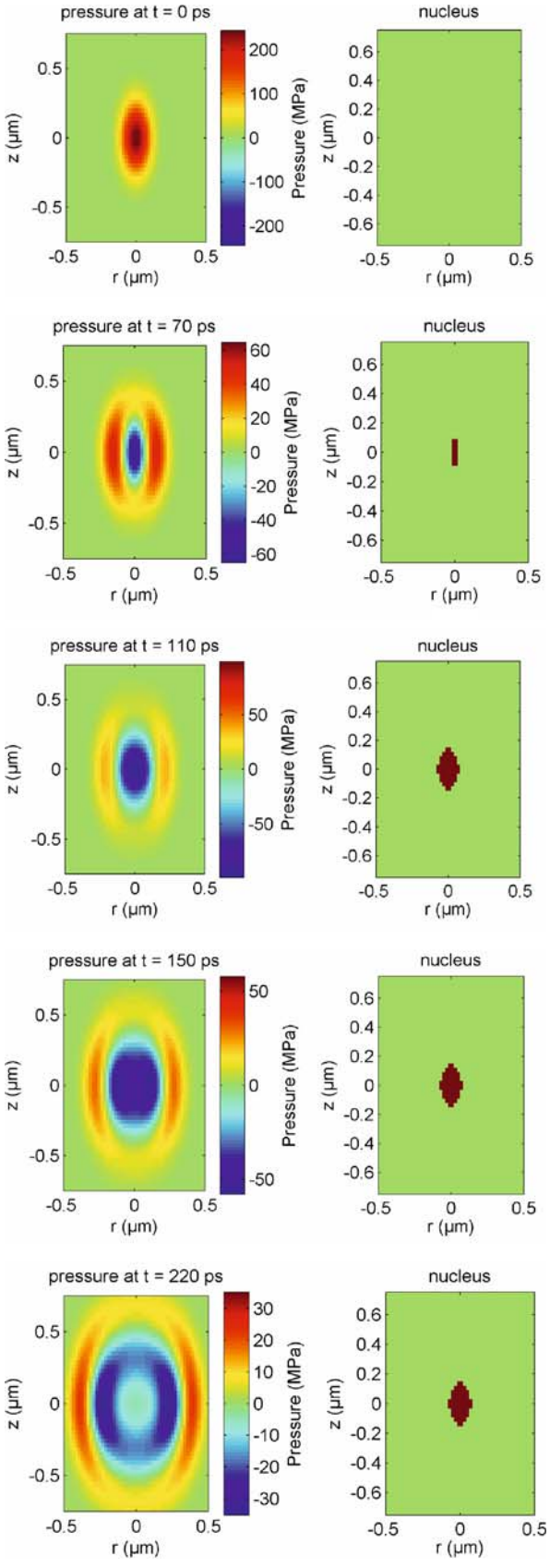

FIGURE 18 Two-dimensional plots of the thermoelastic stress evolution (*left*) and of the region in which the kinetic spinodal limit is exceeded (*right*). This region demarcates the size of the bubble nucleus that is then expanded by the thermoelastic tensile stress wave. The calculations were performed for a peak temperature of 200 °C

where p_0 is the initial thermoelastic pressure generated under conditions of stress confinement and the integration encompasses the entire volume that is heated by the laser pulse. For a temperature rise in the center of the focal volume of 180 °C such as in Fig. 19 that leads to a maximum pressure p_0 of 221 MPa, E_{TE} amounts to 7.8×10^{-14} J. For comparison, the total heat content of the plasma is

$$E_{\mathrm{tot}} = \varrho_0 C_{\mathrm{p}} \int \Delta T \, \mathrm{d}V \,, \tag{23}$$

giving $E_{\mathrm{tot}} = 1.66 \times 10^{-11}$ J under the same conditions. The energetic conversion efficiency from heat into the thermoelastic wave is therefore $E_{\mathrm{TE}}/E_{\mathrm{tot}} = 0.46\%$, and the conversion efficiency from thermoelastic energy into bubble energy is 6.8%. This result of a low conversion efficiency from absorbed laser energy into mechanical energy for femtosecond pulses is in agreement with experimental results [80, 128]. By contrast, for nanosecond optical breakdown with NA = 0.9 the conversion efficiency was experimentally found to be 12.7% for $\lambda = 1064$ nm and 3.3% for $\lambda = 532$ nm at the breakdown threshold, and it reached values of 53% and 33.5%, respectively, for energies 10-fold above threshold [3].

Experimental data on cavitation bubble dynamics. Time-resolved investigations of the effects of transient femtosecond-laser-induced bubbles on cells are not yet available. However, Dayton et al. investigated the oscillations of 1.5-μm-radius bubbles that were phagocytosed by leukocytes and stimulated by a rarefaction-first one-cycle acoustic pulse with 440 ns duration [188]. By means of streak photography and high-speed photography with 100 Mill. f/s they observed that phagocytosed bubbles expanded about 20%–45% less than free microbubbles in response to a single acoustic pulse of the same intensity. The difference is due to the viscosity of the cytoplasm and the elastic modulus of the cytoskeleton. Bubbles subjected to a tensile-stress amplitude of 0.9 MPa would expand to a radius of 6 μm without rupturing the cell membrane. Larger oscillations would cause immediate cell lysis. The viability of the non-lysed cells after insonation was not tested, but it is evident that the bubble oscillations strain the cell membrane and deform or even rupture the cytoskeleton. In the case of femtosecond optical breakdown, the radius of the bubble nucleus is much smaller (≈ 90 nm compared to 1.5 μm), and the tensile-stress transient acting on the bubbles is much shorter than in the case investigated by Dayton (≈ 100 ps compared to 220 ns). Therefore, the resulting bubbles cause little structural damage within a cell and do not affect cell viability.

Lin et al. investigated the thresholds for cell death produced by cavitation induced around absorbing microparticles irradiated by nanosecond laser pulses [189, 190]. They observed that an energy of 3 nJ absorbed by a single particle of 1-μm diameter produced sufficiently strong cavitation to kill a trabecular meshwork cell after irradiation with a single laser pulse. Pulses with 1-nJ absorbed energy produced lethality after several exposures [189]. Viability was lost even when no morphological damage was apparent immediately after the collapse of the transient bubble with less than 1-μs lifetime (according to the Rayleigh equation [96, 191], 1-μs lifetime corresponds to $R_{\mathrm{max}} = 5.5$ μm). Nuclear

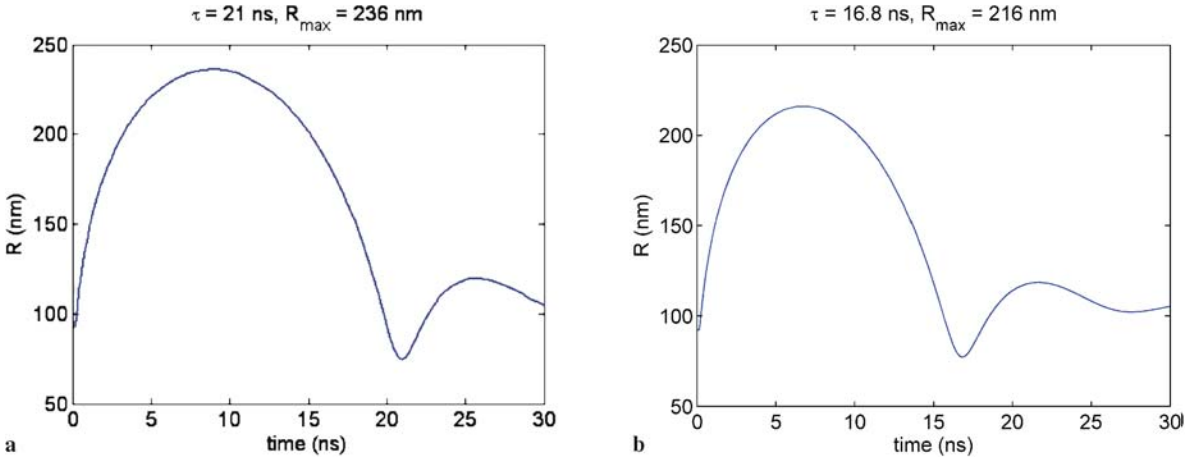

FIGURE 19 Radius–time curve of the cavitation bubble produced by a single femtosecond laser pulse focused at NA = 1.3 that leads to a peak temperature of $T_{max} = 200\,^{\circ}C$ at the focus center. The radius of the bubble nucleus is $R_0 = 91.1$ nm. The temperature at the wall of the nucleus is $T_{wall} = 145\,^{\circ}C$, and the mean temperature averaged over all volume elements within the bubble nucleus is $T_{mean} = 168\,^{\circ}C$. The $R(t)$ curve in (**a**) was calculated under the assumption that the vapor pressure within the bubble is given by the mean temperature within the nucleus and decays due to heat diffusion (case 1, see text). The curve in (**b**) was calculated assuming that the vapor pressure drops adiabatically during bubble expansion (case 2)

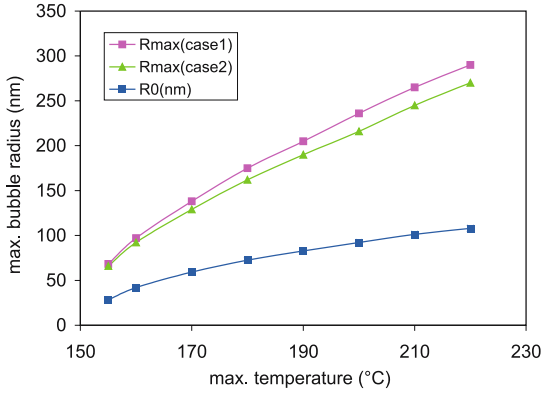

FIGURE 20 Maximum bubble radii for cases 1 and 2 as a function of the maximum temperature achieved in the center of the focal volume, together with the radius of the nucleus, R_0

staining of non-viable cells by ethidium bromide confirmed that cell death was associated with membrane damage. According to Neumann and Brinkmann [192], a bubble radius of 3 μm within a cell of 7.5-μm radius is sufficient to cause an enlargement of the membrane by 4% that will result in membrane rupture [193]. The results of our calculations in Fig. 20 demonstrate that the radius of fs-laser-produced transient bubbles remains well below this damage threshold. This applies even for laser pulse energies of a few nanojoules because for $\varrho_{cr} = 10^{21}\ cm^{-3}$ and 1-μm plasma length about 99% of the incident energy is transmitted through the focal region [81]. The heated volume is much smaller than the volume of the microparticles investigated by Lin et al. [189], and the deposited heat energy corresponding to a peak temperature of $T_{max} = 200\,^{\circ}C$ or $300\,^{\circ}C$ is only 16.6 or 25.8 pJ, respectively, much less than in Lin's case.

Bubbles around gold nanoparticles are of interest in the context of nanoparticle cell surgery (Sect. 1.1). When particles with 4.5-nm radius were irradiated by 400-nm, 50-fs pulses, bubbles of up to 20-nm radius were observed by means of X-ray scattering techniques [194]. The small size of these bubbles, which is one order of magnitude less than for those produced by focused femtosecond laser pulses, is consistent with the fact that the collective action of a large number of nanoparticles is required to produce the desired surgical effect.

Membrane damage can also be induced by bubble oscillations that occur largely outside the cell [195], such as in laser optoporation [50]. Rupture (or at least poration) of the cell membrane requires strains larger than 2%–3% [193, 196]. Again, no time-resolved investigations of the laser-based procedure are yet available, but cell poration and lysis induced by the dynamics of pressure-wave-excited bubbles have already been studied [197]. These effects are of interest in the context of transient membrane permeabilization of cells for the transfer of genes or other substances.

So far, we have only discussed the transient bubbles produced by single laser pulses. These bubbles can only be detected by very fast measurement schemes. However, during high-repetition-rate pulse series accumulative thermal effects and chemical dissociation of biomolecules come into play (Sects. 4 and 5.2) that can produce long-lasting bubbles that are easily observable under the microscope [86, 88, 89]. Dissociation of biomolecules may provide inhomogeneous nuclei that lower the bubble-formation threshold below the superheat limit defined by the kinetic spinodal. Even though thermoelastic forces may still support the bubble growth, it is mainly driven by boiling of cell water and by chemical or thermal decomposition of biomolecules into small volatile fragments. After the end of the fs pulse train, the vapor will rapidly condense but the volatile decomposition products will disappear only by dissolution into the surrounding liquid and thus form a longer-lasting bubble.

Long-lasting 'residual' bubbles have also been observed after pulse series of 3.8-kHz repetition rate where, according to our results Sect. 5.2, accumulative thermal effects can be excluded, but they were seen only when fairly large pulse energies of $\geq$ 180 nJ were applied [198]. The experiments were performed using a numerical aperture of NA = 0.6. Our temperature calculations revealed that, at this NA, the energy required to produce any specific temperature rise is 22.7 times

larger than for NA = 1.3. Therefore, the thermal and chemical effects of single pulses are sufficiently strong to produce a certain amount of non-condensable gas by disintegration of the biomolecules. Rectified diffusion of dissolved air into the oscillating transient bubbles will further contribute to the formation of residual, long-lasting bubbles (see Refs. [199, 200] and Ref. [201], Chap. 6).

7 Implications for laser effects on biological cells and tissues

Two parameter regimes have been established for femtosecond laser nanosurgery: one technique uses long pulse series from fs oscillators with repetition rates of the order of 80 MHz and pulse energies well below the optical breakdown threshold [4, 37, 53, 55, 77, 86, 89, 95, 98]. From 40 000 pulses [4] to several million pulses [53, 77] have been applied at one specific location to achieve the desired dissection or membrane permeabilization. The other approach uses amplified pulse series at 1-kHz repetition rate with pulse energies slightly above the threshold for transient bubble formation [79, 83, 84]. Here the number of pulses applied at one location varied between 30 [83] and several hundred [79, 84].

Based on the discussion of the physical effects associated with femtosecond-laser-induced plasma formation in the previous sections, we now proceed to explain the working mechanisms of both modalities for cell surgery. For this purpose, the different low-density plasma effects and physical breakdown phenomena are summarized in Fig. 21, together with experimental damage, transfection, and dissection thresholds on cells. The different effects are scaled by the corresponding values of free-electron density and irradiance.

Chemical cell damage (2) refers to membrane dysfunction and DNA strand breaks leading to apoptosis-like cell death observed after scanning irradiation of PtK2 cells with 800-nm pulses at 80-MHz repetition rate [144]. Chromosome dissection (3) relates to the intranuclear chromosome dissection [4], and (4) to cell transfection by transient membrane permeabilization [53], both performed using 80-MHz pulse trains from a femtosecond oscillator. Mitochondrion ablation (8) refers to the ablation of a single mitochondrion in a living cell using 1-kHz pulse trains [85], and axon dissection (9) applies to axotomy in live *C. elegans* worms carried out with sequences of pulses emitted at 1-kHz repetition rate from a regenerative amplifier [79]. Points (1), (5), (6) and (7) stand for physical events or threshold criteria. The respective laser parameters and the absolute values of irradiance and free-electron density for each point are listed in Table 2.

7.1 *Femtosecond pulse trains at MHz repetition rates with energies below the threshold for bubble formation*

The irradiance threshold (2) for cell death induced by laser pulse series of 80-MHz repetition rate scanned over the entire cell volume ($0.067 \times I_{\mathrm{rate}}$) is lower than the irradiance threshold for intracellular dissection (3). However, this does not imply that intracellular dissection with 80-MHz pulse series must lead to severe cell damage, because locally confined irradiation does not affect cell viability in the same way as scanning irradiation.

The threshold for intranuclear chromosome dissection with 80-MHz pulse series (3) is almost four times as large as the irradiance (1) producing one free electron per pulse in the focal volume ($0.15 \times I_{\mathrm{rate}}$ vs $0.04 \times I_{\mathrm{rate}}$). In fact, about 1000 free electrons per pulse are produced with the parameters used for dissection. Therefore, it is very likely

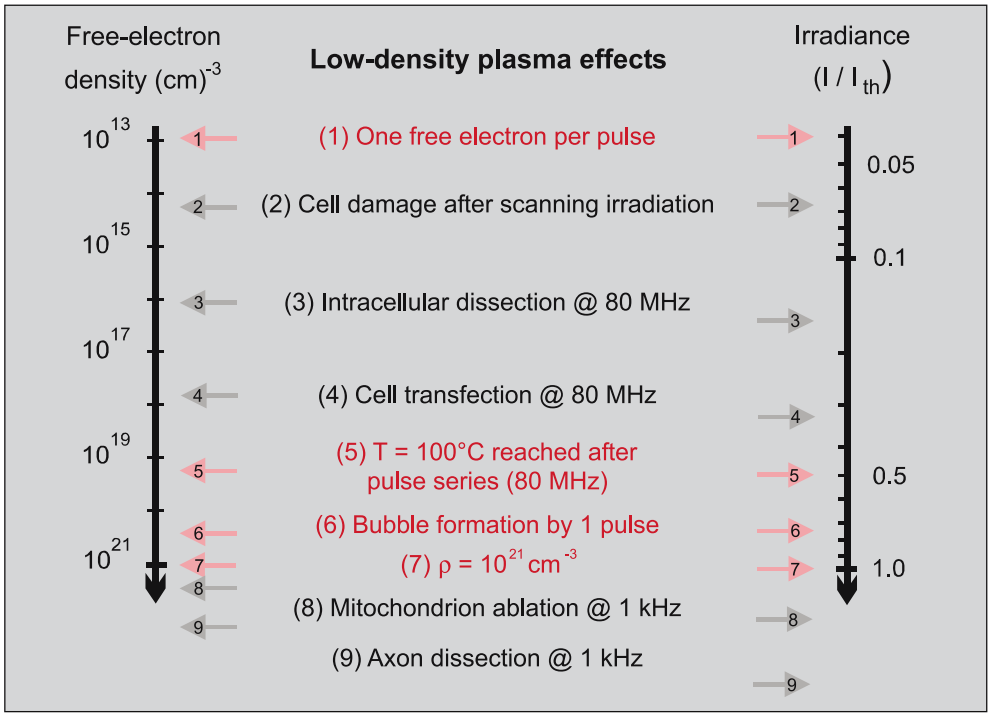

FIGURE 21 Overall view of physical breakdown phenomena induced by femtosecond laser pulses, together with experimental damage, transfection, and dissection thresholds for cells. The different effects are depicted together with the corresponding values of free-electron density and irradiance. The irradiance values are normalized to the optical breakdown threshold I_{th} defined by a critical electron density of $\varrho_{\mathrm{cr}} = 10^{21}\ \mathrm{cm}^{-3}$. All data refer to plasma formation in water with femtosecond pulses of about 100-fs duration and 800-nm wavelength; the exact pulse durations are given in Table 2

Effect	Pulse duration (fs) NA	Energy (nJ)	Repetition rate	Dwell time (ms) Average power	Number of pulses per spot	Electron density (cm^{-3})	Volum. energy density ($J\,cm^{-3}$)	Irradiance ($\times 10^{12}$ $W\,cm^{-2}$)	Normalized irradiance I/I_{rate}
(1) One free electron per pulse	100 1.3		Single pulse	–	1	2.1×10^{13}	4.9×10^{-5}	0.26	0.04
(2) Chemical cell damage after scanning irrad. [144]	90 1.3	0.0875	80 MHz	0.6 per cell 7 mW	4.8×10^4 per cell	1.5×10^{14}	3.5×10^{-4} for one pulse	0.44	0.067
(3) Intranuclear chromosome dissection at 80 MHz [4]	170 1.3	0.38	80 Mhz	0.5 per chromosome dissection 30 mW	4×10^4	2.0×10^{16}	4.7×10^{-2} for one pulse	1.0	0.15
(4) Cell transfection at 80 MHz [53]	170 1.3	0.6–1.2	80 MHz	12 50–100 mW	9.6×10^5	5–200 $\times 10^{17}$	1.2–47 for one pulse	1.6–3.1	0.25–0.48
(5) ΔT of 100 °C after many pulses	100 1.3		80 MHz	≥ 0.1	$\geq 0.8 \times 10^4$	2.1×10^{19}	50 for one pulse	3.3	0.51
(6) Bubble formation in pure water	100 1.3		Single pulse	–	1	2.36×10^{20}	551	5.1	0.78
(7) Bd threshold in numerical models	100			–	1	1.0×10^{21}	2.6×10^3	6.54	1
(8) EYFP-tagged mitochondrion ablation at 1 kHz [85]	100 1.4	2	1 kHz	> 100	Several hundred	$\geq 10^{21}$	$\geq 2.6 \times 10^3$	10.5	1.6
(9) Axon dissection in *C. elegans* at 1 kHz [79]	200 1.4	10	1 kHz	400	400	$\geq 10^{21}$	$\geq 2.6 \times 10^3$	52	8.0

TABLE 2 Numerical values of the data presented in Fig. 21. All data refer to a laser wavelength of $\lambda = 800$ nm, and water as breakdown medium. The experimental irradiance values assume diffraction-limited focusing conditions and a perfect laser beam. They refer to the peak irradiance in the laser focus ($\approx 2\times$ average irradiance within the spot diameter) to make them comparable with the calculated values. The actual irradiance in the experiments is probably somewhat smaller than the values calculated under these assumptions. For superthreshold irradiance values, the plasma will grow in size, and plasma shielding and reflection will limit the growth of the free-electron density. Therefore, no exact values of the electron density and energy density are given

that the intracellular ablation produced by long trains of femtosecond pulses in the low-density plasma regime relies on cumulative free-electron-mediated chemical effects. This hypothesis is supported by the facts that the individual pulses produce a thermoelastic tensile stress of only ≈ 0.014 MPa, and a pulse series of 100-μs duration results in a temperature rise of only ≈ 0.076 °C. These values for tensile stress and temperature rise are far too small to cause any cutting effect or other type of cell injury. The breaking of chemical bonds, as described in Sect. 4, may first lead to a disintegration of the structural integrity of biomolecules and finally to a dissection of sub-cellular structures. Bond breaking may be initiated both by resonant interactions with low-energy electrons, and by multiphoton processes of lower order that do not yet create free electrons [4, 202–204].

Interestingly, transient membrane permeabilization for gene transfer (4) requires a considerably larger laser dose than chromosome dissection. Not only is the irradiance larger, but the number of applied pulses ($\approx 10^6$) also far exceeds the quantity necessary for chromosome dissection ($\approx 4 \times 10^4$). Chromosome dissection may be facilitated by the DNA absorption around 260 nm enabling nonlinear absorption through lower-order multiphoton processes. Moreover, while breakage of relatively few bonds is sufficient for chromosome dissection, the creation of a relatively large opening is required for diffusion of a DNA plasmid through the cell membrane. The corresponding laser parameters are still within the regime of free-electron-mediated chemical effects but already quite close to the range where cumulative heat effects start to play a role (5).

At larger laser powers, bubbles with a lifetime of the order of a few seconds were observed that probably arise from dissociation of biomolecules into volatile, non-condensable fragments [86, 88, 89, 205]. This dissociation of relatively large amounts of biomaterials can be attributed both to free-electron chemical and photochemical bond breaking as well as to accumulative thermal effects. The appearance of the bubbles is an indication of severe cell damage or cell death within the targeted region and defines an upper limit for the laser power suitable for nanosurgery. A criterion for successful intratissue dissection at lower energy levels is the appearance of intense autofluorescence in perinuclear cell regions [86, 88] that is likely due to the destruction of mitochondria at the rim of the laser cut [98].

7.2 *Femtosecond pulses at kHz repetition rates with energies above the bubble-formation threshold*

When pulse trains of 1-kHz repetition rate are employed for nanosurgery, pulse energies in the range 2–40 nJ are used [79, 83–85]. Examples are the ablation of single mitochondria (8) by several hundred 2-nJ pulses [85] and the severing of axons in a live *C. elegans* worm (9) with a similar number of 10-nJ pulses [79]. These energies are above the threshold for thermoelastically induced formation of minute transient cavitation bubbles (6), and are thus associated with mechanical disruption effects. The tensile thermoelastic stress waves enable dissection of cellular structures at low volumetric energy densities, and the small size of the heated volume (Fig. 8) correlates with a radius of the expanded bubble of the order of only 120–300 nm (Fig. 20). This explains why fs-laser-induced bubble formation does not necessarily lead to cell damage whereas ns-laser-induced bubble generation is usually associated with cell death [61, 189, 190, 192, 206].

Due to the contribution of mechanical effects to dissection, the total energy required for nanosurgery with kHz pulse series is less than the total energy necessary with MHz pulse trains. For example, ablation of a mitochondrion using 1-kHz pulses required a total energy of less than 1 μJ [85], while for intranuclear chromosome dissection with 80-MHz pulses an energy of 15 μJ was needed [4].

For sufficiently large pulse energies, bubble expansion and shock-wave pressure can cause effects far beyond the focal volume, which lead to cell death [83, 198, 207]. To avoid unwanted side effects, irradiances should be used that are only slightly above the bubble-formation threshold. Useful techniques for an on-line monitoring of the ablation threshold during laser surgery are to detect the onset of photobleaching, or of light scattering by bubbles generated at the laser focus. Heisterkamp et al. found that the threshold for photobleaching is just below the ablation threshold [84]. Neumann and Brinkmann described a light-scattering technique for an on-line detection of micrometer-sized bubbles produced by pulsed laser irradiation [208].

We conclude that, depending on the repetition rate of the fs laser pulses, nanosurgery relies on two very different mechanisms. With oscillator pulse trains at MHz repetition rates, dissection is due to accumulative chemical effects in low-density plasmas. In this regime, no transient bubbles with sub-microsecond lifetime are produced, and the formation of long-lived bubbles by accumulative chemical and thermal effects must be avoided. With pulse trains at kHz repetition rates, the accumulative creation of chemical effects would take too long to be practical. Therefore, the pulse energies are raised to a level where the thermoelastic generation of minute transient bubbles enables us to achieve nanodissections. Due to their short lifetime of less than 100 ns and the long time intervals between the laser pulses, no cumulative bubble growth occurs as long as pulse energies close to the bubble-formation threshold are used.

7.3 *Comparison with long-pulsed and cw irradiation*

In their pioneering work, Berns et al. [69, 70] used high-power argon-laser irradiation in multiline operation (with wavelengths of 488 nm and 514 nm) applied in 25–30-μs pulses. Other researchers employed longer exposure times of 0.25 s [47] and 1 to 2.5 s [52] at smaller laser power. Berns et al. [34] related the spatial extent of their laser effects simply to the irradiance distribution in the focal region. However, with the exposure times used, the energy deposition is broadened by thermal diffusion. For large numerical apertures the focal volume has an almost spherical shape, and the characteristic thermal diffusion time t_d is approximately given as [124]

$$t_d = d^2/8\kappa\,, \tag{24}$$

where κ is the thermal diffusivity and d the focal diameter. Thermal confinement of the energy deposition requires that the laser exposure is shorter than the thermal diffusion time [2]. For a focal spot diameter of 480 nm in aqueous media ($\lambda = 514$ nm, NA = 1.3), this is the case only for laser pulse durations < 210 ns; for longer laser exposures such as used by Berns et al. [34] the temperature distribution is broadened. We have seen in Sect. 5.3 (Fig. 12) that the distribution close to the focus center becomes stationary after about 10 μs. This implies that the spatial extent of effects from laser pulses longer than 10 μs is similar to that of lesions arising from cw laser irradiation. Nevertheless, the temperature distribution is very narrow even for cw irradiation, because from a point-like source the heat can diffuse in all spatial directions and, therefore, the temperature drops very quickly with growing distance from the source.

Effects created by long-pulsed or cw irradiation usually rely on linear (one-photon) absorption. For argon-laser irradiation at wavelengths of 488 nm and 514 nm that can be well transmitted into a cell, the laser power needed for surgery in unstained cells exceeds 1 W [70]. It is thus considerably higher than the average power of about 30 mW necessary with femtosecond laser pulse trains at 800 nm [4, 37], for which plasma formation induced by the ultra-short laser pulses results in a dramatic local increase of the absorption coefficient at the focus, regardless of the linear absorption coefficient. Berns et al. speculated that high-power argon-laser cell surgery is most likely a multiphoton mechanism [34]. However, even though two-photon-excited visible fluorescence was observed in experiments with a 760-nm cw laser beam [209], multiphoton absorption is unlikely to be the dominant absorption mechanism considering the fact that the focal irradiance for 1-W laser power (5.5×10^8 W cm^{-2} is three orders of magnitude less than the irradiance required for intracellular dissection with 800-nm, 170-fs pulses. The focal irradiance used for quasi-cw cell surgery is also much lower than the irradiances used for multiphoton microscopy [210, 211]. Thus, there is little doubt that quasi-cw cell surgery is based on the linear absorption in the target structures, whereas ultra-short-pulsed surgery relies on nonlinear absorption.

It was shown above that no purely thermal effects can be produced using ultra-short laser pulses. All thermal effects are accompanied by free-electron-mediated chemical effects and thermoelastic mechanical effects. By contrast, quasi-cw cell surgery is mediated by local thermolysis and the formation of minute vapor bubbles. The temperatures required for thermolysis depend on the heat-exposure time [212], and are well above 100 °C for heat-exposure durations in the millisec-

ond or microsecond range [57, 213]. The bubble-nucleation threshold by thermolysis of strongly absorbing biomolecules such as melanin was found to be about 150 °C for pulse durations between 12 ns and 1.8 μs [208]. This seems to be the lower temperature limit of cell surgery using microsecond pulses. The upper limit of a localized temperature rise without bubble formation is given by the threshold for explosive vaporization in the entire focal volume that for non-pigmented cells was found to be about 220 °C [213]. This threshold is lower than the superheat limit of water at ambient pressure (≈ 300 °C) above which homogeneous nucleation and spinodal decomposition will result in a phase explosion [2, 159, 163], probably because of the heterogeneous structure of the cells.

The temperatures required for quasi-cw cell surgery are considerably higher than those involved in femtosecond laser dissection by high-repetition-rate fs pulse trains that relies on photochemical and free-electron-mediated chemical effects (Sect. 7.1). They are in a similar range as the temperatures needed for femtosecond laser surgery at repetition rates below 1 MHz that is based on bubble formation by tensile thermoelastic stress (Sect. 7.2).

The spatial resolution of quasi-cw cell surgery is related to the temperature distribution arising from a continuous deposition of laser energy via linear absorption that was presented in Fig. 11. Interestingly, it is not much broader than the temperature distribution arising from nonlinear absorption of femtosecond pulse trains shown in Fig. 10. However, as the spatial resolution of femtosecond laser surgery is given by the width of the free-electron distribution rather than by the temperature distribution, the precision of the energy deposition in fs laser surgery is considerably better than for cw or long-pulsed irradiation. The half-width of the free-electron distribution shown in Fig. 8b for $\lambda = 800$ nm and NA = 1.3 is only 190 nm in the radial direction, compared to the half-widths of 590 nm and 730 nm of the temperature distributions in Fig. 11 resulting from irradiation with pulse durations of 10 μs and 10 ms, respectively. It should be mentioned, however, that thermal damage is not directly proportional to the temperature elevation but to the damage integral that is an exponential function of temperature [212]. The thermally damaged region can therefore be narrower than the half-width of the temperature distribution [42, 214]. Because of this reason, the gain of spatial resolution achievable by use of ultra-short laser pulses instead of quasi-cw irradiation is less than often assumed. Using fs pulses, extracellular chromosomes could be completely dissected with an FWHM cut size of about 300 nm, which amounts to 40% of the diffraction-limited focal spot size [37]. Berns et al. produced chromosomal lesions of less than 1-μm size using argon-laser irradiation [34]. Thus, the spatial resolution achieved by IR femtosecond laser surgery is a factor of about three better than that of the classical technique introduced more than 30 years ago [69].

A major advantage of femtosecond laser surgery is that it can be performed at arbitrary locations even in media that are transparent at low irradiances, and with much less average power. The use of low-power argon lasers requires staining of the target structures [34, 47, 52, 69]. The need for staining reduces the versatility of the technique compared to femtosecond laser surgery that can be performed at any arbitrary location. Another important advantage of ultra-short laser irradiation is the option to combine material modification with high-resolution nonlinear imaging modalities.

Recently, Paterson et al. reported that cell-wall permeabilization is possible with a low-power blue diode laser ($\lambda = 405$ nm) using 0.3-mW irradiation and 40-ms exposure time [56]. Owing to the short laser wavelength, the energy used (13 μJ) was three orders of magnitude less than the energy required for membrane permeabilization with 488-nm irradiation [52]. It was more than one order of magnitude larger than the energy of 0.5 μJ needed with ns pulses [48], but the transfection process with millisecond pulses avoids mechanical disruptions extending beyond the region of the laser focus that are a problem with ns pulses [3]. Mechanical disruption was also avoided in the study by Tirlapur and König who used 80-MHz femtosecond pulse trains of 800 nm for membrane permeabilization [53], but the total energy employed was here about 50 times larger than with the blue diode laser. Considering the fact that a blue laser diode is less costly than a femtosecond laser, the practical advantages of ultra-short laser pulses for membrane permeabilization still have to be proven. However, ultra-short laser pulses are the tool of choice for intracellular and intratissue nanosurgery at arbitrary locations and/or in conjunction with nonlinear imaging.

7.4 *Potential hazards from low-density plasmas in multiphoton microscopy and second-harmonic imaging*

A matter of concern is that low-density plasmas could be a potential hazard in multiphoton microscopy [203, 210, 215–217] and higher-harmonic imaging [86, 218–221]. Multiphoton imaging of cells is usually done using femtosecond laser pulses of about 700–1100-nm wavelength emitted at ≈ 80 MHz from an oscillator with mean powers of 100 μW up to several milliwatts [210, 211]. Similar mean powers are required for second-harmonic imaging [220]. These laser powers are close to the threshold for cell damage reported to be between 2 mW and 10 mW depending on the damage criterion used, the pulse duration, and the number of applied pulses [4, 82, 98, 144, 202, 203]. They are also close to the values used for intracellular and intratissue dissection that range from 4 to 100 mW, depending on target structure [4, 53, 55, 77, 86, 88]. This suggests that the mechanisms underlying laser cell surgery may also contribute to the side effects in nonlinear imaging.

Our results indicate that thermal damage can be ruled out as a cause of cell damage in multiphoton microscopy as even dissection with oscillator pulses does not involve thermal effects (Fig. 21), and previous studies confirm this finding [222, 223]. In the literature, photodamage produced by short laser pulses is mostly ascribed to multiphoton-induced photochemistry [72, 82, 224]. However, a comparison of the irradiance thresholds for photodamage with the corresponding free-electron densities in Fig. 21 shows that the formation of low-density plasmas may contribute considerably to the observed damage or even dominate its creation, especially in non-stained targets. An exception is the work of Berns et al. [224], who achieved gene manipulation by exposing chromosomes that were sensitized with a dye absorbing

at 530-nm wavelength to 100-ps pulses of 1064-nm wavelength. The peak irradiance used in these experiments was $\approx 10^7$ W/cm^2, far below the threshold for plasma formation, and it is quite clear that in this case the laser effects relied on two-photon-induced photochemical changes without the involvement of free electrons. By contrast, the irradiance required to induce localized DNA damage in non-stained chromosomes or cell nuclei was $\approx 10^{11}$ W/cm^2 for 5.7-ns pulses of 532-nm wavelength [73] and 1.9×10^{11} W/cm^2 for 120-fs pulses of 750-nm wavelength [82]. The first irradiance value is larger than the optical breakdown threshold in water at the same pulse duration that was measured to be 0.77×10^{11} W/cm^2 [3]. In the second case, a three-photon interaction can provide the energy required for molecular excitation at the DNA absorption peak around 260 nm, but the irradiance required for photodamage will also generate a free-electron density of $\approx 10^{13}$ cm^{-3}, which borders the region in which chemical changes may be induced by pulse series. Eggeling et al. [204] showed that the photobleaching kinetics with femtosecond laser pulses usually involves excitation into higher electronic states close to the ionization threshold followed by photolysis, unlike for longer pulse durations where photobleaching occurs via the triplet state. Heisterkamp et al. [84] found that slightly larger irradiance values than those required for photobleaching lead to ablation, a process mediated by plasma formation. Together these findings indicate that low-density plasmas may be involved in the generation of ultra-short-laser-induced effects that were traditionally exclusively attributed to direct photochemical reactions, and may also contribute to photodamage in nonlinear microscopy. With increasing irradiance, free-electron-mediated chemical effects become ever more important compared to direct photochemical reactions because the rate of free-electron generation increases very fast with irradiance due to its high-order nonlinearity.

We saw that multiphoton fluorescence excitation bears a trade-off between low off-focus and severe in-focus photobleaching [204]. This raises the question of which laser pulse duration, repetition rate, and wavelength are best suited to minimize the detrimental effects. It was found that at the same level of photodamage pulses with 3–4-ps duration provide the same signal or even an increase in signal compared to femtosecond pulses [202, 203, 217]. The increase in signal is due to the fact that, at constant irradiance, longer pulses produce a larger fluorescence excitation yield. The smaller fluorescence yield associated with the use of shorter pulses could be compensated for by an increase in peak power if the irradiance dependences of photodamage and multiphoton ionization were the same. However, the irradiance dependence of photodamage is usually steeper than that of multiphoton excitation [72, 202, 203], because photodamage often involves higher-order photochemical effects or even ionization. Therefore, the use of very short high-intensity femtosecond pulses for nonlinear imaging involves a larger risk of photodamage and seems to be neither essential nor advantageous. A prolongation of the pulse duration is, on the other hand, associated with an increase of average power because the peak power of the individual pulses cannot be reduced without loss of multiphoton excitation efficiency. The upper limit of useful pulse durations is set by the average power level leading to cumulative thermal damage. In aqueous media with low absorption coefficient in the wavelength range around 800 nm cumulative thermal damage is not produced for power levels up to at least 100 mW [70, 223].

Similar considerations apply for the selection of optimum repetition rates for nonlinear imaging. The limit for the maximum useful repetition rate is defined by the rate of energy deposition for which thermal damage starts to occur. This rate depends on the NA of the microscope objective (Figs. 10 and 11), and on the linear absorption coefficient of the cells or tissues investigated. The limit is especially low in pigmented tissues such as skin [205], but in non-pigmented tissues and cells even GHz repetition rates may be used. When for pulses of constant peak power of the individual pulses the laser repetition rate was increased from 80 MHz to 2 GHz, a much better signal to noise ratio could be achieved within the same image-acquisition time [220]. GHz repetition rates can also be employed to achieve the same signal strength with considerably smaller pulse peak power than with 80 MHz. This increases the safety margin with respect to photodamage [220] and is thus of special interest for in-vivo nonlinear microscopy.

In second- and third-harmonic imaging, the use of longer IR wavelengths than 800 nm was found to be advantageous because with a longer wavelength more photons are required for ionization and thus the safety margin increases [86, 220]. Also with regard to multiphoton microscopy, it is advantageous to use fluorophores with long excitation wavelengths that enable the use of longer laser wavelengths. In this way, the order of the multiphoton process can remain the same for imaging while the number of photons required for ionization increases. However, if a specific fluorophore with a given excitation wavelength must be employed, the orders of the nonlinearities involved in image formation and photodamage increase in a similar fashion with increasing wavelength. Therefore, the optimum wavelength must in these cases be determined for each individual fluorophore [77].

8 Summary and conclusions

Femtosecond laser pulses enable the creation of spatially extremely confined chemical, thermal, and mechanical effects in biological media and other transparent materials via free-electron generation through nonlinear absorption. Because of the nonlinear nature of plasma formation and the deterministic relationship between free-electron density and irradiance, effect sizes well below the diffraction limit can be achieved. Precision and versatility are better than with cw irradiation, for which the energy deposition relies on one-photon absorption and vital stains are often required to create the necessary absorption.

Free electrons are produced in a fairly large irradiance range below the optical breakdown threshold. This low-density plasma regime provides a ‘tuning range’ in which the nature of the laser-induced effects can be deliberately changed by gradually varying the irradiance. Chemical effects induced by the free electrons and direct multiphoton interactions dominate at the lower end of this irradiance range, whereas at the upper end they are mixed with thermal effects and modified by thermoelastic stresses. For a sufficiently

strong temperature rise, the thermoelastic tensile stress leads to bubble formation, and the laser-induced effects become more disruptive. The threshold for bubble formation defines the experimental breakdown criterion for aqueous media. In our investigations performed for a numerical aperture of NA = 1.3, it corresponds to a temperature rise of 131.5 °C and an end temperature of 151.5 °C, well below the superheat threshold. It was reached with a free-electron density of $\varrho_c = 0.236 \times 10^{21}$ cm^{-3}, which is below the threshold criterion of $\varrho_{cr} = 10^{21}$ cm^{-3} commonly used in the modeling of plasma formation.

Although it is convenient to distinguish between chemical, thermal, and thermomechanical effects, a clear separation between these regimes does not exist for femtosecond laser effects. Because free-electron generation precedes any thermal or thermomechanical effects, the latter are never independent of free-electron-induced chemistry or multiphoton-induced photochemical effects. Temperatures that would usually lead to thermal denaturation are associated with millions of free electrons in the focal volume that produce chemical changes.

The stress confinement of the energy deposition in femtosecond-laser-induced material processing is responsible for the generation of large compressive and tensile stress amplitudes at a moderate temperature rise. Therefore, a temperature rise of as little as 131.5 °C is sufficient for bubble generation in a liquid without any pre-existing nuclei. The low volumetric energy density required for thermoelastically induced cavity formation (only about 1/5 of the vaporization enthalpy) is a reason for the lack of thermal side effects in femtosecond laser dissection and the small conversion rate of laser energy into mechanical energy. Moreover, it explains why at the bubble-formation threshold the bubble size is much smaller than for 'conventional' phase transitions without stress confinement.

Based on the analysis of the laser-induced chemical and physical effects, we investigated the working mechanisms of femtosecond laser nanoprocessing in biomaterials with oscillator pulses of 80-MHz repetition rate and with amplified pulses of 1-kHz repetition rate and revealed that they belong to two different regimes. Dissection at 80-MHz repetition rate is performed in the low-density plasma regime at subnanojoule energies well below the optical breakdown threshold and less than one order of magnitude higher than those used for nonlinear imaging. It is mediated by free-electron-induced chemical decomposition (bond breaking) in conjunction with multiphoton-induced chemistry, and hardly related to heating or thermoelastic stresses. Dissection with 1-kHz repetition rate is performed using about 10-fold larger pulse energies (a few nanojoules) and relies on thermoelastically induced formation of minute transient cavities that is probably facilitated by the free-electron-induced decomposition of biomolecules and by direct photochemistry.

Unwanted side effects in femtosecond laser surgery are usually related to the formation of long-lasting bubbles in the high-repetition-rate mode that are produced by accumulative heating and tissue dissociation into volatile fragments, and to excessively large transient bubbles in the low-repetition-rate mode. Future experiments must explore the specific hazards of each side effect and define the respective 'therapeutic range' for each surgical modality.

The use of oscillator pulse trains is technically simpler and offers the possibility of combining nonlinear material modification with nonlinear imaging. Amplified pulses allow us not only to perform nanosurgery but are also suited for tasks requiring larger cutting rates and pulse energies, such as the precise dissection of individual cells from histological specimens and their subsequent separation by laser catapulting, or the non-destructive isolation of single cultured cells [225–227]. They are probably also more suitable for high-throughput cell transfection.

Short wavelengths seem to be especially well suited for the manipulation of cellular events because the dependence of the free-electron density on irradiance is weak and the tuning range between chemical, thermal, and mechanical effects is thus broader than for longer wavelengths. Short wavelengths in the visible or UVA portion of the optical spectrum provide, furthermore, better spatial resolution than infrared wavelengths. However, if simultaneous nonlinear material modification and nonlinear imaging is desired, one needs to use IR wavelengths because they have a larger optical penetration depth and enable us to produce multiphoton-induced fluorescence, second-harmonic generation, or third-harmonic generation within a well-detectable wavelength range. The largest safety margin for nonlinear imaging without deleterious side effects for the specimen exists when the difference in the order of the multiphoton effects used for imaging and ionization is as large as possible, which is the case for IR wavelengths > 1000 nm.

The principal mechanisms of femtosecond laser interaction with biomaterials described above are not only relevant for nanosurgery with tightly focused laser pulses but also for applications such as intrastromal corneal refractive surgery [11–14] or presbyopia treatment [228], where the laser pulses are focused at smaller numerical apertures. In the latter cases, nonlinear beam propagation must be taken into account, and one needs to bear in mind that the thermoelastic tensile stress amplitude produced by energy deposition into cylindrical volumes differs from those arising from spherical or ellipsoidal volumes [155]. Similar considerations also apply for the analysis of intraocular lesions from ultra-short laser pulses in the context of laser safety [183, 229, 230].

Besides nanoprocessing of biological materials, low-density plasmas can also be used to modify other transparent materials and enable, for example, the generation of optical waveguides, couplers, or even lasers in bulk glass and fused silica [5–8]. The process of plasma formation in the bulk of other dielectrics like fused silica and glass strongly resembles the process in water [5, 116, 123, 231]. Variations are mainly due to differences in the band-gap energy, which is 6.5 eV for water but ≈ 4 eV for barium aluminum borosilicate (BBS) and 9.0 eV for fused silica [123, 232]. The material response to plasma formation will, of course, be modified by the different threshold values for chemically and thermomechanically induced changes. However, the methods employed in this paper for the analysis of femtosecond laser effects in water can also be used to study the effects created in solid dielectrics. When pulse series with high repetition rate are used, low-density plasmas may lead to the formation of defects or color centers that are associated with a change of the refractive index [233, 234]. Thermal effects produced

through heat accumulation during application of series of femtosecond pulses may also play a role [231, 235], but cannot be separated from and are probably dominated by the chemical effects of the free electrons. Thermal effects, and especially the resulting thermoelastic stresses, will play a prominent role for low repetition rates and larger pulse energies [236–238], where they can even lead to the formation of voids [179, 235, 239]. Void formation in solid dielectrics requires a larger plasma energy density than bubble formation in aqueous media but, due to the strongly nonlinear energy deposition, only a slight increase in irradiance. This explains the similarity of the optical breakdown thresholds for both groups of materials.

We conclude that with the advent of compact and reliable femtosecond laser technology, nanoprocessing of biological cells and tissues has gained new exciting perspectives. A deeper understanding of the working mechanisms will help to further optimize this technique, to open new avenues for micro- and nanomanipulation, and to find new applications for functional studies on cells and small organisms.

An important challenge for future research is the time-resolved investigation of the laser-induced events, especially for those cases where bubble formation is involved in dissection, and the assessment of the consequences of the bubbles' oscillations for the integrity, metabolism, and viability of the affected cells. To achieve optimum precision and predictability of effects produced at 1 kHz and allow for on-line dosimetry, techniques for real-time feedback on the formation of transient bubbles with lifetimes of 1 μs or smaller must be established. A measurement of the bubble oscillation amplitude will also allow us to determine their size and thus to assess the potential damage range of the laser effects. For surgery using oscillator pulses at MHz repetition rates, bubble oscillations are probably not relevant. Here, bubble growth is a much slower process driven by the cumulative production of non-condensable gas and can more easily be monitored.

A significant shortcoming of all present models of optical breakdown in biomaterials is the lack of consideration of the specific absorption properties of the biomolecules or stains contained in the aqueous medium. Future models should consider the role of heating by linear absorption and the modification of multiphoton processes by intermediate energy levels located within the band gap for water. These levels could allow for multiphoton processes of lower order, leading to free-electron generation and bond breaking in the biomolecule at lower irradiances than those required for optical breakdown of water.

ACKNOWLEDGEMENTS This work was sponsored by the US Air Force Office of Scientific Research through its European Office of Aerospace Research and Development under Grant No. FA8655-02-1-3047, and, in parts, by the German Bundesministerium für Bildung und Forschung under Grant No. 13N8461. We appreciate stimulating discussions on the modeling of plasma formation with Paul Kennedy (US Air Force Optical Research Laboratory, Brooks City Base, San Antonio, USA), Nadezhda Bulgakova (Institute of Thermophysics, SB RAS, Novosibirsk, Russia), Rieko Verhagen (Philips Research, Eindhoven, The Netherlands), Cord Arnold (Laserzentrum Hannover, Germany), and Norbert Linz (Institute of Biomedical Optics, University of Lübeck, Germany). We thank S.B. Kiselev (Colorado School of Mines, Golden, USA) for providing tabulated data of the kinetic spinodal [163] used for calculating the bubble-formation thresholds.

REFERENCES

1 Y.R. Shen, *The Principles of Nonlinear Optics* (Wiley, New York 1984)
2 A. Vogel, V. Venugopalan, Chem. Rev. **103**, 577 (2003)
3 V. Venugopalan, A. Guerra, K. Nahen, A. Vogel, Phys. Rev. Lett. **88**, 078 103 (2002)
4 K. König, I. Riemann, P. Fischer, K. Halbhuber, Cell. Mol. Biol. **45**, 195 (1999)
5 C.B. Schaffer, A. Brodeur, J.F. García, E. Mazur, Opt. Lett. **26**, 93 (2001)
6 K. Minoshima, A.M. Kowalevicz, I. Hartl, E. Ippen, J.G. Fujimoto, Opt. Lett. **26**, 1516 (2001)
7 W. Watanabe, T. Asano, K. Yamada, K. Itoh, J. Nishii, Opt. Lett. **28**, 2491 (2003)
8 S. Taccheo, G. Della Valle, R. Osellame, G. Cerullo, N. Chiodo, P. Laporta, O. Svelto, A. Killi, U. Morgner, M. Lederer, D. Kopf, Opt. Lett. **29**, 2626 (2004)
9 R.F. Steinert, C.A. Puliafito, *The Nd:YAG Laser in Ophthalmology* (Saunders, Philadelphia 1986)
10 A. Vogel, W. Hentschel, J. Holzfuss, W. Lauterborn, Ophthalmology **93**, 1259 (1986)
11 I. Ratkay-Traub, I.E. Ferincz, T. Juhasz, R.M. Kurtz, R.R. Krueger, J. Refract. Surg. **19**, 94 (2003)
12 A. Heisterkamp, T. Mamom, O. Kermani, W. Drommer, H. Welling, W. Ertmer, H. Lubatschowski, Graef. Arch. Clin. Exp. **241**, 511 (2003)
13 T. Juhasz, F.H. Loesel, R.M. Kurtz, C. Horvath, J.F. Bille, G. Mourou, IEEE J. Sel. Top. Quantum Electron. **5**, 902 (1999)
14 M. Han, L. Zickler, G. Giese, M. Walter, F.H. Loesel, J.F. Bille, J. Biomed. Opt. **9**, 760 (2004)
15 A. Vogel, K. Nahen, D. Theisen, IEEE J. Sel. Top. Quantum Electron. **2**, 847 (1996)
16 A. Heisterkamp, T. Ripken, H. Lubatschowski, T. Mamom, W. Drommer, H. Welling, W. Ertmer, Appl. Phys. B **74**, 419 (2002)
17 W. Liu, O. Kosareva, I.S. Golubtsov, A. Iwasaki, A. Becker, V.P. Kandidov, S.L. Chin, Appl. Phys. B **76**, 215 (2003)
18 S.S. Mao, F. Quéré, S. Guizard, X. Mao, R.E. Russo, G. Petite, P. Martin, Appl. Phys. A **79**, 1695 (2004)
19 J. Kasparian, J. Solle, M. Richard, J.-P. Wolf, Appl. Phys. B **79**, 947 (2004)
20 M. Kolesik, E.M. Wright, J.V. Moloney, Phys. Rev. Lett. **92**, 253 901 (2004)
21 C.L. Arnold, A. Heisterkamp, W. Ertmer, H. Lubatschowski, Appl. Phys. B **80**, 247 (2005)
22 U. Fuchs, U.D. Zeitner, A. Tünnermann, Opt. Express **13**, 3852 (2005)
23 R.K. Saiki, D.H. Gelfand, S. Stoffel, S.J. Scharf, R. Higuchi, G.T. Horn, K.B. Mullis, H.A. Erlich, Science **239**, 487 (1988)
24 A.F. Markham, Brit. Med. J. **306**, 441 (1993)
25 S.A. Bustin, J. Mol. Endocrinol. **25**, 169 (2000)
26 G. Isenberg, W. Bielser, W. Meier-Ruge, E. Remy, J. Microsc. **107**, 19 (1976)
27 W. Meier-Ruge, W. Bielser, E. Remy, F. Hillenkamp, R. Nitsche, R. Unsöld, Histochem. J. **8**, 387 (1976)
28 K. Schütze, H. Pösl, G. Lahr, Cell. Mol. Biol. **44**, 735 (1998)
29 K. Schütze, G. Lahr, Nat. Biotechnol. **16**, 737 (1998)
30 G. Lahr, Lab. Invest. **80**, 1477 (2000)
31 K. Lorenz, Mechanismen des Katapultierens biologischer Strukturen mit UV-Laserpulsen, Diploma Thesis, University of Applied Science Lübeck (2004) [in German]. Accessible through vogel@bmo.uni-luebeck.de
32 C.E. Sims, G.D. Meredith, T.B. Krasieva, M.W. Berns, B.J. Tromberg, N.L. Allbritton, Anal. Chem. **700**, 4570 (1998)
33 K.R. Rau, A. Guerra, A. Vogel, V. Venugopalan, Appl. Phys. Lett. **84**, 2940 (2004)
34 M.W. Berns, J. Aist, J. Edwards, K. Strahs, J. Girton, P. McNeil, J.B. Kitzes, M. Hammer-Wilson, L.-H. Liaw, A. Siemens, M. Koonce, S. Peterson, S. Brenner, J. Burt, R. Walter, P.J. Bryant, D. van Dyk, J. Coulombe, T. Cahill, G.S. Berns, Science **213**, 505 (1981)
35 H. Liang, W.H. Wright, S. Cheng, W. He, M.W. Berns, Exp. Cell Res. **204**, 110 (1993)
36 K.O. Greulich, *Micromanipulation by Light in Biology and Medicine* (Birkhäuser, Basel Boston Berlin 1999)
37 K. König, I. Riemann, W. Fritsche, Opt. Lett. **26**, 819 (2001)
38 S. Sato, E. Higurashi, Y. Taguchi, H. Inaba, Appl. Phys. B **54**, 531 (1992)
39 K. Schütze, A. Clement-Sengewald, Nature **368**, 667 (1994)

40 J. Neev, Y. Tadir, P. Ho, M.W. Berns, R.H. Asch, T. Ord, J. Assist. Reprod. Genet. **9**, 513 (1992)
41 S. Antinori, C. Panci, H.A. Selman, B. Caffa, G. Dani, C. Versaci, Hum. Reprod. **11**, 590 (1996)
42 K. Rink, G. Delacretaz, R. Salathé, A. Senn, D. Noccera, M. Germond, P. De Grandi, S. Fakan, Laser. Surg. Med. **18**, 52 (1996)
43 E. Mantoudis, B.T. Podsiadly, A. Gorgry, G. Venkat, I.L. Craft, Hum. Reprod. **16**, 2182 (2001)
44 M. Tsukakoshi, S. Kurata, Y. Nomiya, Y. Ikawa, T. Kasuya, Appl. Phys. B **35**, 135 (1984)
45 S.-I. Kurata, M. Tsukakoshi, T. Kasuya, Y. Ikawa, Exp. Cell Res. **162**, 372 (1986)
46 W. Tao, J. Wilkinson, E. Stanbridge, M.W. Berns, Proc. Natl. Acad. Sci. USA **84**, 4180 (1987)
47 G. Palumbo, M. Caruso, E. Crescenzi, M.F. Tecce, G. Roberti, A. Colasanti, J. Photochem. Photobiol. B **36**, 41 (1996)
48 T.B. Krasieva, C.F. Chapman, V.J. LaMorte, V. Venugopalan, M.W. Berns, B.J. Tromberg, Proc. SPIE **3260**, 38 (1998)
49 C.S. Buer, K.T. Gahagan, G.S. Swartzlander Jr., P.J. Weathers, Biotechnol. Bioeng. **60**, 348 (1998)
50 J.S. Soughayer, T. Krasieva, S.C. Jacobson, J.M. Ramsey, B.C. Tromberg, N.L. Albritton, Anal. Chem. **72**, 1342 (2000)
51 Y. Shirahata, N. Ohkohchi, H. Itagak, S. Satomi, J. Invest. Med. **49**, 184 (2001)
52 H. Schneckenburger, A. Hendiger, R. Sailer, W.S.L. Strauss, M. Schmitt, J. Biomed. Opt. **7**, 410 (2002)
53 U.K. Tirlapur, K. König, Nature **418**, 290 (2002)
54 S.K. Mohanty, M. Sharma, P. Gupta, Biotechnol. Lett. **25**, 895 (2003)
55 E. Zeira, A. Manevitch, A. Khatchatouriants, O. Pappo, E. Hyam, M. Darash-Yahana, E. Tavor, A. Honigman, A. Lewis, E. Galun, Mol. Ther. **8**, 342 (2003)
56 L. Paterson, B. Agate, M. Comrie, R. Ferguson, T.K. Lake, J.E. Morris, A.E. Carruthers, C.T.A. Brown, W. Sibbett, P.E. Bryant, F. Gunn-Moore, A.C. Riches, K. Dholakia, Opt. Express **13**, 595 (2005)
57 G. Huettmann, R. Birngruber, IEEE J. Sel. Top. Quantum Electron. **5**, 954 (1999)
58 D.G. Jay, T. Sakurai, Biochim. Biophys. Acta **1424**(2–3), M39–M48 (1999)
59 G. Hüttmann, J. Serbin, B. Radt, B. Lange, R. Birngruber, Proc. SPIE **4257**, 398 (2001)
60 S. Beck, T. Sakurai, B. Eustace, G. Beste, R. Schier, F. Rudert, D.G. Jay, Proteomics **2**, 247 (2002)
61 C.M. Pitsillides, E.K. Joe, X. Wei, R.R. Anderson, C.P. Lin, Biophys. J. **84**, 4023 (2003)
62 C.P. Yao, R. Rahmanzadeh, E. Endl, Z. Zhang, J. Gerdes, G. Hüttmann, J. Biomed. Opt. **10** (2005) in press
63 S. Tschachotin, Biol. Zentralbl. **32**, 623 (1912)
64 M. Bessis, G. Nomarski, J. Biophys. Biochem. Cy. **8**, 777 (1960)
65 G. Moreno, M. Lutz, M. Bessis, Int. Rev. Exp. Pathol. **7**, 99 (1969)
66 M. Bessis, F. Gires, G. Mayer, G. Nomarski, C. R. Acad. Sci. III – Vie **255**, 1010 (1962)
67 R.L. Amy, R. Storb, Science **150**, 756 (1965)
68 R. Storb, R.L. Amy, R.K. Wertz, B. Fauconnier, M. Bessis, J. Cell Biol. **31**, 11 (1966)
69 M.W. Berns, R.S. Olson, D.E. Rounds, Nature **221**, 74 (1969)
70 M.W. Berns, W.K. Cheng, A.D. Floyd, Y. Ohnuki, Science **171**, 903 (1971)
71 O.G. Stonington, T.P. Spurck, J.A. Snyder, J.D. Picket-Heaps, Protoplasma **153**, 62 (1989)
72 M. Bessis, Adv. Biol. Med. Phys. **13**, 209 (1971)
73 P.P. Calmettes, M.W. Berns, Proc. Natl. Acad. Sci. USA **80**, 7197 (1983)
74 A. Khodjakov, R.W. Cole, C.L. Rieder, Curr. Biol. **10**, 59 (2000)
75 J. Colombelli, S.W. Grill, E.H.K. Stelzer, Rev. Sci. Instrum. **75**, 472 (2004)
76 E.L. Botvinick, V. Venugopalan, J.V. Shah, L.H. Liaw, M. Berns, Biophys. J. **87**, 4203 (2004)
77 L. Sacconi, I.M. Tolic-Norrelyke, R. Antolini, F.S. Pavone, J. Biomed. Opt. **10**, 014 002 (2005)
78 J.R. Aist, H. Liang, M.W. Berns, J. Cell Sci. **104**, 1207 (1993)
79 M.F. Yanik, H. Cinar, H.N. Cinar, A.D. Chisholm, Y. Jin, A. Ben-Yakar, Nature **432**, 822 (2004)
80 A. Vogel, J. Noack, K. Nahen, D. Theisen, S. Busch, U. Parlitz, D.X. Hammer, G.D. Nojin, B.A. Rockwell, R. Birngruber, Appl. Phys. B **68**, 271 (1999)
81 J. Noack, A. Vogel, IEEE J. Quantum Electron. **35**, 1156 (1999)
82 R.A. Meldrum, S.W. Botchway, C.W. Wharton, G.J. Hirst, EMBO Rep. **12**, 1144 (2003)
83 W. Watanabe, N. Arakawa, S. Matsunaga, T. Higashi, K. Fukui, K. Isobe, K. Itoh, Opt. Express **12**, 4203 (2004)
84 A. Heisterkamp, I.Z. Maxwell, E. Mazur, J.M. Underwood, J.A. Nickerson, S. Kumar, D.E. Ingber, Opt. Express **13**, 3690 (2005)
85 N. Shen, D. Datta, C.B. Schaffer, P. LeDuc, D.E. Ingber, E. Mazur, Mech. Chem. Biosyst. **2**, 17 (2005)
86 W. Supatto, D. Dèbarre, B. Moulia, E. Brouzés, J.-L. Martin, E. Farge, E. Beaurepaire, Proc. Natl. Acad. Sci. USA **102**, 1047 (2005)
87 S.H. Chung, D.A. Clark, C.V. Gabel, E. Mazur, A.D.T. Samuel, J. Neurosci. **25** (2005) in press
88 K. König, O. Krauss, I. Riemann, Opt. Express **10**, 171 (2002)
89 I. Riemann, T. Anhut, F. Stracke, R. Le Harzic, K. König, Proc. SPIE **5695**, 216 (2005)
90 A.A. Oraevsky, L.B. Da Silva, A.M. Rubenchik, M.D. Feit, M.E. Glinsky, M.D. Perry, B.M. Mammini, W. Small IV, B. Stuart, IEEE J. Sel. Top. Quantum Electron. **2**, 801 (1996)
91 A. Vogel, J. Noack, Proc. SPIE **4260**, 83 (2001)
92 A. Khodjakov, R.W. Cole, B.R. Oakley, C.L. Rieder, Cell Motil. Cytoskel. **38**, 311 (1997)
93 S.W. Grill, J. Howard, E. Schäffer, E.H.K. Stelzer, A.A. Hyman, Science **301**, 518 (2003)
94 J. Colombelli, E.G. Reynaud, J. Rietdorf, R. Pepperkork, E.H.K. Stelzer, Traffic **6**, 1093 (2005)
95 N.I. Smith, K. Fujita, T. Kaneko, K. Katoh, O. Nakamura, S. Kawata, T. Takamatsu, Appl. Phys. Lett. **79**, 1208 (2001)
96 A. Vogel, S. Busch, U. Parlitz, J. Acoust. Soc. Am. **100**, 148 (1996)
97 A. Vogel, J. Noack, G. Hüttmann, G. Paltauf, Proc. SPIE **4633**, 23 (2002)
98 H. Oehring, I. Riemann, P. Fischer, K.J. Halbhuber, K. König, Scanning **22**, 263 (2000)
99 F. Docchio, C.A. Sachhi, J. Marshall, Lasers Ophthalmol. **1**, 83 (1986)
100 C.A. Sacchi, J. Opt. Soc. Am. B **8**, 337 (1991)
101 F. Williams, S.P. Varama, S. Hillenius, J. Chem. Phys. **64**, 1549 (1976)
102 D. Grand, A. Bernas, E. Amouyal, Chem. Phys. **44**, 73 (1979)
103 D.N. Nikogosyan, A.A. Oraevsky, V. Rupasov, Chem. Phys. **77**, 131 (1983)
104 L.V. Keldysh, Sov. Phys. JETP **20**, 1307 (1965)
105 M.V. Ammosov, N.B. Delone, V.P. Krainov, Sov. Phys. JETP **64**, 1191 (1986)
106 J.F. Ready, *Effects of High Power Laser Radiation* (Academic, Orlando 1971), p. 261
107 K.K. Thornber, J. Appl. Phys. **52**, 279 (1981)
108 D. Arnold, E. Cartier, Phys. Rev. B **46**, 15 102 (1992)
109 B.K. Ridley, *Quantum Processes in Semiconductors* (Oxford University Press, Oxford 1999)
110 P.K. Kennedy, IEEE J. Quantum Electron. **31**, 2241 (1995)
111 Q. Feng, J.V. Moloney, A.C. Newell, E.M. Wright, K. Cook, P.K. Kennedy, D.X. Hammer, B.A. Rockwell, C.R. Thompson, IEEE J. Quantum Electron. **33**, 127 (1997)
112 A.C. Tien, S. Backus, H. Kapteyn, M. Murnane, G. Mourou, Phys. Rev. Lett. **82**, 3883 (1999)
113 A. Kaiser, B. Rethfeld, M. Vicanek, G. Simon, Phys. Rev. B **61**, 11 437 (2000)
114 L.V. Keldysh, Sov. Phys. JETP **11**, 509 (1960)
115 B. Rethfeld, Phys. Rev. Lett. **92**, 187 401 (2004)
116 B.C. Stuart, M.D. Feit, S. Hermann, A.M. Rubenchik, B.W. Shore, M.D. Perry, Phys. Rev. B **53**, 1749 (1996)
117 N. Bloembergen, IEEE J. Quantum Electron. **10**, 375 (1974)
118 Q. Sun, H. Jiang, Y. Liu, Z. Wu, H. Yang, Q. Gong, Opt. Lett. **30**, 320 (2005)
119 A.P. Joglekar, H. Liu, G.J. Spooner, E. Meyhöfer, G. Mourou, A.L. Hunt, Appl. Phys. B **77**, 25 (2003)
120 A.P. Joglekar, H. Liu, E. Meyhöfer, G. Mourou, A.L. Hunt, Proc. Nat. Acad. Sci. **101**, 5856 (2004)
121 M.D. Feit, A.M. Komashko, A.M. Rubenchik, Appl. Phys. A **79**, 1657 (2004)
122 D.X. Hammer, R.J. Thomas, G.D. Noojin, B.A. Rockwell, P.A. Kennedy, W.P. Roach, IEEE J. Quantum Electron. **3**, 670 (1996)
123 M. Lenzner, J. Krüger, S. Sartania, Z. Cheng, C. Spielmann, G. Mourou, W. Kautek, F. Krausz, Phys. Rev. Lett. **80**, 4076 (1998)
124 H.S. Carslaw, J.C. Jaeger, *Conduction of Heat in Solids*, 2nd edn. (Oxford University Press, Oxford 1959)
125 F. Docchio, Europhys. Lett. **6**, 407 (1988)

126 K. Nahen, A. Vogel, IEEE J. Sel. Top. Quantum Electron. **2**, 861 (1996)
127 J. Noack, Optischer Durchbruch in Wasser mit Laserpulsen zwischen 100 ns und 100 fs, Ph.D. Dissertation, University of Lübeck (1998)
128 J. Noack, D.X. Hammer, G.D. Noojin, B.A. Rockwell, A. Vogel, J. Appl. Phys. **83**, 7488 (1998)
129 D. Du, X. Liu, G. Mourou, Appl. Phys. B **63**, 617 (1996)
130 D. Du, J. Squier, R. Kurtz, V. Elner, X. Liu, G. Güttmann, G. Mourou, in *Ultrafast Phenomena IX*, ed. by P.F. Barbara, W.H. Knox, G.A. Mourou, A.H. Zewail (Springer, New York 1994), p. 254
131 D. Stern, R.W. Schoenlein, C.A. Puliafito, E.T. Dobi, R. Birngruber, J.G. Fujimoto, Arch. Ophthalmol. – Chic. **107**, 587 (1989)
132 M.H. Niemz, T.P. Hoppeler, T. Juhasz, F.J. Bille, Lasers Light Ophthalmol. **5**, 149 (1993)
133 T.P. Hughes, *Plasmas and Laser Light* (Adam Hilger, Bristol 1975)
134 R.P. Godwin, C.G.M. van Kessel, J.N. Olsen, P. Sachsenmaier, R. Sigel, Z. Naturforsch. **32a**, 1100 (1977)
135 D. von der Linde, H. Schüler, J. Opt. Soc. Am. B **13**, 216 (1996)
136 D.X. Hammer, E.D. Jansen, M. Frenz, G.D. Noojin, R.J. Thomas, J. Noack, A. Vogel, B.A. Rockwell, A.J. Welch, Appl. Opt. **36**, 5630 (1997)
137 C.H. Fan, J. Sun, J.P. Longtin, J. Appl. Phys. **91**, 2530 (2002)
138 C.H. Fan, J. Sun, J.P. Longtin, J. Heat Trans. – T. ASME **124**, 275 (2002)
139 D.M. Rayner, A. Naumov, P.B. Corkum, Opt. Express **13**, 3208 (2005)
140 M. Born, E. Wolf, *Principles of Optics* (Pergamon Press, Oxford 1970)
141 H. Ditlbacher, J.R. Krenn, A. Leitner, F.R. Aussenegg, Opt. Lett. **29**, 1408 (2004)
142 S. Grill, E.H.K. Stelzer, J. Opt. Soc. Am. A **16**, 2658 (1999)
143 B.C. Garret, D.A. Dixon, D.M. Camaioni, D.M. Chipman, M.A. Johnson, C.D. Jonah, G.A. Kimmel, J.H. Miller, T.N. Rescigno, P.J. Rossky, S.S. Xantheas, S.D. Colson, A.H. Laufer, D. Ray, P.F. Barbara, D.M. Bartels, K.H. Becker, K.H. Bowen, S.E. Bradforth, I. Carmichael, J.V. Coe, L.R. Corrales, J.P. Cowin, M. Dupuis, K.B. Eisenthal, J.A. Franz, M.S. Gutowski, K.D. Jordan, B.D. Kay, J.A. LaVerne, S.V. Lymar, T.E. Madey, C.W. McCurdy, D. Meisel, S. Mukamel, A.R. Nilsson, T.M. Orlando, N.G. Petrik, S.M. Pimblott, J.R. Rustad, G.K. Schenter, S.J. Singer, A. Tokmakoff, L.S. Wang, C. Wittig, T.S. Zwier, Chem. Rev. **105**, 355 (2005)
144 U.K. Tirlapur, K. König, C. Peuckert, R. Krieg, K.-J. Halbhuber, Exp. Cell Res. **263**, 88 (2001)
145 B. Boudaiffa, P. Cloutier, D. Hunting, M.A. Huels, L. Sanche, Science **287**, 1658 (2000)
146 H. Hotop, in L.G. Christophorou, J.K. Olthoff (eds.), *Proceedings of the International Symposium on Gaseous Dielectrics IX*, Ellicott City, MD, USA, 22–25 May 2001 (Kluwer Academic/Plenum, New York, 2001), p. 3
147 S. Gohlke, E. Illenberger, Europhys. News **33**, 207 (2002)
148 M.A. Huels, B. Boudaiffa, P. Cloutier, D. Hunting, L. Sanche, J. Am. Chem. Soc. **125**, 4467 (2003)
149 T. Mitchinson, M. Kirschner, Nature **312**, 237 (1984)
150 I.M. Jánosi, D. Chrétien, H. Flyvberg, Biophys. J. **83**, 1317 (2002)
151 H.O. Jeschke, E.M. Garcia, in *Nonlinear Optics, Quantum Optics and Ultrafast Phenomena with X-rays*, ed. by B.W. Adams (Kluwer Academic, Boston Dordrecht London 2003), p. 175
152 N.M. Bulgakova, R. Stoian, A. Rosenfeld, I.V. Hertel, E.E.B. Campbell, Phys. Rev. B **69**, 054 102 (2004)
153 S. Nolte, C. Momma, H. Jacobs, A. Tünnermann, B.N. Chikov, B. Wellegehausen, H. Welling, J. Opt. Soc. Am. B **14**, 2716 (1997)
154 H. Kuchling, *Taschenbuch der Physik*, 13th edn. (Fachbuchverlag Leipzig 1991)
155 G. Paltauf, H. Schmidt-Kloiber, Appl. Phys. A **68**, 525 (1999)
156 G. Paltauf, P. Dyer, Chem. Rev. **103**, 487 (2003)
157 M.W. Sigrist, F.K. Kneubühl, J. Acoust. Soc. Am. **64**, 1652 (1978)
158 G. Paltauf, H. Schmidt-Kloiber, Appl. Phys. A **62**, 303 (1996)
159 V.P. Skripov, E.N. Sinitsin, P.A. Pavlov, G.V. Ermakov, G.N. Muratov, N.V. Bulanov, V.G. Baidakov, *Thermophysical Properties of Liquids in the Metastable (Superheated) State* (Gordon and Breach, New York 1988)
160 K.P. Köstli, M. Frenz, H. Bebie, H.P. Weber, Phys. Med. Biol. **46**, 1863 (2001)
161 B.T. Cox, P.C. Beard, J. Acoust. Soc. Am. **117**, 3616 (2005)
162 C.E. Brennen, *Cavitation and Bubble Dynamics* (Oxford University Press, New York Oxford 1995)
163 S.B. Kiselev, Physica A **269**, 252 (1999)
164 S.B. Kiselev, J.F. Ely, Physica A **299**, 357 (2001)
165 P.G. Debenedetti, *Metastable Liquids: Concepts and Principles* (Princeton University Press, Princeton 1996)
166 J.C. Fisher, J. Appl. Phys. **19**, 1062 (1948)
167 Q. Zheng, D.J. Durben, G.H. Wolf, C.A. Angell, Science **254**, 829 (1991)
168 B. Garrison, T.E. Itina, L.V. Zhigilei, Phys. Rev. E **68**, 041 501 (2003)
169 F.R. Gilmore, Calif. Inst. Tech. Rep. 26 (1952)
170 R.T. Knapp, J.W. Daily, F.G. Hammitt, *Cavitation* (McGraw-Hill, New York 1971), pp. 117–131
171 J. Staudenraus, W. Eisenmenger, Ultrasonics **31**, 267 (1993)
172 G. Paltauf, H. Schmidt-Kloiber, J. Appl. Phys. **82**, 1525 (1997)
173 J. Noack, A. Vogel, Appl. Opt. **37**, 4092 (1998)
174 M.H. Rice, J.M. Walsh, J. Chem. Phys. **26**, 824 (1957)
175 P.A. Barnes, K.E. Rieckhoff, Appl. Phys. Lett. **13**, 282 (1968)
176 J. Stolarski, J. Hardman, C.G. Bramlette, G.D. Noojin, R.J. Thomas, B.A. Rockwell, W.P. Roach, Proc. SPIE **2391**, 100 (1995)
177 E.J. Chapyak, R.P. Godwin, A. Vogel, Proc. SPIE **2975**, 335 (1997)
178 B. Zysset, J.G. Fujimoto, T.F. Deutsch, Appl. Phys. B **48**, 139 (1989)
179 E.N. Glezer, E. Mazur, Appl. Phys. Lett. **71**, 882 (1997)
180 C.B. Schaffer, N. Nishimura, E. Mazur, SPIE Proc. **3451**, 2 (1998)
181 T. Juhasz, G.A. Kastis, C. Suarez, Z. Bor, W.E. Bron, Lasers Surg. Med. **19**, 23 (1996)
182 C.B. Schaffer, N. Nishimura, E.N. Glezer, A.M.-T. Kim, E. Mazur, Opt. Express **10**, 196 (2002)
183 C.P. Cain, R.J. Thomas, G.D. Noojin, D.J. Stolarski, P.K. Kennedy, G.D. Buffington, B.A. Rockwell, Graef. Arch. Clin. Exp. Published online (7 July 2004)
184 A. Vogel, K. Nahen, D. Theisen, R. Birngruber, R.J. Thomas, B.A. Rockwell, Appl. Opt. **38**, 3636 (1999)
185 L.B. Glebov, O.M. Efimov, G.T. Petrovski, P.N. Rogovtsev, Sov. J. Quantum Electron. **15**, 226 (1984)
186 O.M. Efimov, J. Opt. Technol. **71**, 338 (2004)
187 M.J. Soileau, W.F. Williams, N. Mansour, E.W. Van Stryland, Opt. Eng. **28**, 1133 (1989)
188 P.A. Dayton, J.E. Chomas, A.F.H. Lunn, J.S. Allen, J.R. Lindner, S.I. Simon, K.W. Ferrara, Biophys. J. **80**, 1547 (2001)
189 C.P. Lin, M.W. Kelly, S.A.B. Sibayan, M.A. Latina, R.R. Anderson, IEEE J. Sel. Top. Quantum Electron. **5**, 963 (1999)
190 D. Leszczynski, C.M. Pitsillides, R.K. Pastila, R.R. Anderson, C.P. Lin, Radiat. Res. **156**, 399 (2001)
191 Lord Rayleigh, Philos. Mag. **34**, 94 (1917)
192 J. Neumann, R. Brinkmann, Proc. SPIE **5863**, 586 307 (2005)
193 D. Needham, R.S. Nunn, Biophys. J. **58**, 997 (1990)
194 V. Kotaidis, A. Plech, Appl. Phys. Lett. **87**, (2005) in press
195 M. Lokhandwalla, B. Sturtevant, Phys. Med. Biol. **46**, 413 (2001)
196 D. Boal, *Mechanics of the Cell* (Cambridge University Press, Cambridge 2002)
197 B. Wolfrum, R. Mettin, T. Kurz, W. Lauterborn, Appl. Phys. Lett. **81**, 5060 (2002)
198 M.J. Zohdy, C. Tse, J.Y. Ye, M. O'Donnell, IEEE T. Ultrason. Ferr. **52** (2005) in press
199 L.A. Crum, Ultrasonics **22**, 215 (1984)
200 T.G. Leighton, *The Acoustic Bubble* (Academic, London 1994)
201 A. Vogel, *Optical Breakdown in Water and Ocular Media, and Its Use for Intraocular Photodisruption* (Shaker Verlag, Aachen 2001)
202 H.J. Koester, D. Baur, R. Uhl, S.W. Hell, Biophys. J. **77**, 2226 (1999)
203 A. Hopt, E. Neher, Biophys. J. **80**, 2029 (2001)
204 C. Eggeling, A. Volkmer, C.A.M. Seidel, Chem. Phys. Chem. **6**, 791 (2005)
205 B.R. Masters, P.T.C. So, C. Buehler, N. Barry, J.D. Sutin, W.W. Mantulin, E. Gratton, J. Biomed. Opt. **9**, 1265 (2004)
206 J. Roegener, R. Brinkmann, C.P. Lin, J. Biomed. Opt. **9**, 367 (2004)
207 W. Watanabe, S. Matsungata, T. Shimada, T. Higashi, K. Fukui, K. Itoh, Med. Laser Appl. **20**, 185 (2005)
208 J. Neumann, R. Brinkmann, J. Biomed. Opt. **10**, 024 001 (2005)
209 K. König, H. Liang, M.W. Berns, B.J. Tromberg, Nature **377**, 20 (1995)
210 K. König, J. Microsc. **200**, 83 (2000)
211 K. König, in *Methods in Cellular Imaging*, ed. by A. Periasamy (Oxford University Press, Oxford 2001), p. 236
212 J. Pearce, S. Thomsen, in *Optical–Thermal Response of Laser-Irradiated Tissue*, ed. by A.J. Welch, M. van Germert (Plenum, New York 1995), p. 561
213 D. Simanowski, M. Sarkar, A. Irani, C.O'Connel-Rodwell, C. Contag, A. Schwettman, D. Palanker, Proc. SPIE **5695**, 254 (2005)

214 L. Descloux, S. Rastegar, G. Delacretaz, A. Hollis, K. Rink, Proc. SPIE **3195**, 137 (1998)
215 W.J. Denk, J.H. Strickler, W.W. Webb, Science **248**, 73 (1990)
216 P.T.C. So, Opt. Express **3**, 312 (1998)
217 K. König, T.W. Becker, P. Fischer, I. Riemann, K.J. Halbhuber, Opt. Lett. **24**, 113 (1999)
218 Y. Guo, P.P. Ho, A. Tirksliunas, F. Liu, R.R. Alfano, Opt. Lett. **22**, 1323 (1997)
219 L. Moreaux, O. Sandre, J. Mertz, J. Opt. Soc. Am. B **17**, 1685 (2000)
220 S.-W. Chu, T.M. Liu, C.-K. Sun, C.-Y. Lin, H.-J. Tsai, Opt. Express **11**, 933 (2003)
221 L. Fu, X. Gan, M. Gu, Opt. Lett. **30**, 385 (2005)
222 W.J. Denk, D.W. Piston, W.W. Webb, in *Handbook of Biological Confocal Microscopy*, ed. by J.B. Prawley (Plenum, New York 1995), p. 445
223 A. Schönle, S. Hell, Opt. Lett. **23**, 325 (1998)
224 M.W. Berns, Z. Wang, A. Dunn, V. Wallace, V. Venugopalan, Proc. Natl. Acad. Sci. USA **97**, 9504 (2000)
225 Y. Hosokawa, H. Takabayashi, S. Miura, C. Shukunami, Y. Hiraki, H. Masuhara, Appl. Phys. A **79**, 795 (2004)
226 J.A. Barron, P. Wu, H.D. Ladouceur, B.R. Ringeisen, Biomed. Microdev. **6**, 139 (2004)
227 B.R. Ringeisen, H. Kim, J.A. Barron, D.B. Krizman, D.B. Chrisey, S. Jackman, R.Y.C. Auyeung, B.J. Spargo, Tissue Eng. **10**, 483 (2004)
228 T. Ripken, U. Oberheide, C. Ziltz, W. Ertmer, G. Gerten, H. Lubatschowski, Proc. SPIE **5688**, 278 (2005)
229 C.A. Toth, D.G. Narayan, G.D. Noojin, K.P. Winter, B.A. Rockwell, W.P. Roach, Invest. Ophth. Vis. Sci. **38**, 2204 (1997)
230 B.A. Rockwell, D.X. Hammer, R.A. Hopkins, D.J. Payne, C.A. Toth, W.P. Roach, J.J. Druessel, P.K. Kennedy, R.E. Amnotte, B. Eilert, S. Phillips, G.D. Noojin, D.J. Stolarski, C. Cain, J. Laser Appl. **11**, 42 (1999)
231 C.B. Schaffer, J.F. García, E. Mazur, Appl. Phys. A **71**, 351 (2003)
232 M. Bass (ed. in chief), *Handbook of Optics*, vol. II (McGraw-Hill, New York 1995)
233 O.M. Efimov, K. Gabel, S.V. Garnov, L.B. Glebov, S. Grantham, M. Richardson, M.J. Soileau, J. Opt. Soc. Am. B **15**, 193 (1998)
234 A. Hertwig, S. Martin, J. Krüger, W. Kautek, Appl. Phys. A **79**, 1075 (2004)
235 W. Watanabe, T. Toma, K. Yamada, J. Nishii, K. Hayashi, K. Itoh, Opt. Lett. **25**, 1669 (2000)
236 A.M. Streltsov, N.F. Borelli, J. Opt. Soc. Am. B **19**, 2496 (2002)
237 B. Poumellec, L. Sudrie, M. Franco, B. Prade, A. Mysyrowicz, Opt. Express **9**, 1070 (2003)
238 V.R. Bhardwaj, P.B. Corkum, D.M. Rayner, C. Hnatowsky, E. Simova, R.S. Taylor, Opt. Lett. **29**, 1312 (2004)
239 S. Juodkazis, K. Yamasaki, V. Mizeikis, S. Matsuo, H. Misawa, Appl. Phys. A **79**, 1549 (2004)
240 A. Saul, W. Wagner, J. Phys. Chem. Ref. Data **18**, 1537 (1989)